

# Diversity of Type Ia supernova optical light curves among different spectroscopic subclasses

Ryotaro B. KOSHI,<sup>1</sup> Mamoru DOI,<sup>2</sup> Shigeyuki SAKO,<sup>1</sup> Keiichi MAEDA,<sup>3</sup> Masaomi TANAKA,<sup>4,5</sup> and Naohiro TAKANASHI<sup>6</sup>

<sup>1</sup>Institute of Astronomy, Graduate School of Science, The University of Tokyo, 2-21-1 Osawa, Mitaka, Tokyo 181-0015

<sup>2</sup>National Astronomical Observatory of Japan, 2-21-1 Osawa, Mitaka, Tokyo 181-8588

<sup>3</sup>Department of Astronomy, Kyoto University, Kitashirakawa-Oiwake-cho, Sakyo-ku, Kyoto 606-8502

<sup>4</sup>Astronomical Institute, Graduate School of Science, Tohoku University, Sendai 980-8578

<sup>5</sup>Division for the Establishment of Frontier Sciences, Organization for Advanced Studies, Tohoku University, Sendai 980-8577

<sup>6</sup>Executive Management Program, The University of Tokyo, 7-3-1 Hongo, Bunkyo-ku, Tokyo 113-8654

\*E-mail: koshi@ioa.s.u-tokyo.ac.jp

## Abstract

Attempts to reveal the spectroscopic diversity of Type Ia supernovae (SNe Ia) have led to subclassification schemes such as the Branch system, which classifies SNe Ia into four categories: core normal (CN), broad line (BL), cool (CL), and shallow silicon (SS). The physical origin of these spectroscopic differences, including progenitor channels, explosion mechanisms, or other parameters, however, remains unclear. Moreover, previous work has concentrated primarily on properties near peak luminosity, yielding limited insight into their behavior at later epochs. In this study, we compile *UBVRI* photometry for 109 SNe Ia and construct the first set of average light curves for each Branch subgroup, spanning from pre-maximum through the late tail. We find pronounced diversity in the *I*-band, especially in the timing of the secondary maximum across subgroups and in the late-time decline of CL events. After correcting for light curve stretch, which reflects the combined influence of <sup>56</sup>Ni and ejecta masses, we show that the secondary maximum is powered by Fe II recombination, and its timing is particularly sensitive to the amount of stable iron-group elements (IGEs) synthesized in the explosion. This implies an anti-correlation between the mass of stable IGEs and <sup>56</sup>Ni: CL (and possibly BL) events have a larger mass ratio of IGEs/<sup>56</sup>Ni resulting in earlier secondary maxima, while SS events have a smaller ratio and thus later secondary maxima. This trend is naturally explained within the near-*M*<sub>Ch</sub> delayed-detonation scenario, whereas it is inconsistent with the positive correlation predicted by the sub-*M*<sub>Ch</sub> double-detonation scenario. Finally, we show that stretch-corrected late-time slopes provide a practical diagnostic for CL events, likely linked to an emission feature around 7,200 Å.

**Keywords:** supernovae: general — method: data analysis — surveys

## 1 Introduction

Type Ia supernovae (SNe Ia) are thermonuclear explosions of carbon-oxygen white dwarfs (WDs) that exhibit a characteristic Si II absorption feature in their optical spectra at maximum light. SNe Ia are widely believed to arise from a mass-accreting white dwarf in a binary system, but the nature of the companion star remains uncertain. Two leading scenarios are considered today; in the single-degenerate scenario (e.g., Whelan & Iben 1973; Nomoto 1982), a non-degenerate star transfers mass onto the WD until it ignites, whereas in the double-degenerate channel (e.g., Iben & Tutukov 1984; Webbink 1984), the merger of two WDs triggers the explosion.

Besides the progenitor problem, the explosion mechanism itself remains under debate and is an independent factor in understanding the nature of SNe Ia. In classical models, deflagration starts near the center of the WD when the density reaches  $\sim 10^9 \text{ g cm}^{-3}$  and then shifts to detonation (delayed-detonation model; Woosley & Weaver 1995; Iwamoto et al. 1999; Seitenzahl et al. 2013). However, an alternative model claims that detonation can occur at lower WD masses and densities, triggered by an initial detonation at the surface helium-rich layer (double-detonation model; Kromer et al. 2010; Shen & Bildsten 2014; Polin et al. 2019).

Recent multi-dimensional simulations have further highlighted that, in the delayed-detonation model, the relative strengths of deflagration and detonation are antagonistic: stronger initial deflagration leads to greater pre-expansion, which reduces the efficiency of the subsequent detonation and lowers the <sup>56</sup>Ni yield (Krueger et al. 2010; Maeda et al. 2010c; Lach et al. 2022). In addition, enhanced burning at high densities during strong deflagration promotes electron captures, resulting in larger amounts of stable iron-group elements such as <sup>58</sup>Ni and <sup>54</sup>Fe (Blondin et al. 2022).

Note that the explosion mechanism is not uniquely determined by the progenitor channel; even with the companion identified, how ignition and detonation proceed remains uncertain (see Maeda & Terada 2016 for a review). Connecting observations to theoretical models provides crucial constraints on both fronts, making the observed diversity of SNe Ia a central theme in current research.

Studies of photometric diversity have long underpinned our understanding and standardization of SNe Ia. The stretch–magnitude relation is an empirical correlation between the stretch of the light curve (or in some studies, the decline rate) and peak absolute magnitude, showing that slowly declining SNe Ia are intrinsically brighter (Phillips 1993). Another correlation stands between the color at peak luminosity and the peak absolute magnitude; bluer

SNe Ia appear more luminous (Tripp 1998). These relations both potentially illuminate underlying explosion physics, such as the mass of synthesized  $^{56}\text{Ni}$ , and enable calibration of SN Ia luminosity, establishing their use in observational cosmology (Riess et al. 1998; Perlmutter et al. 1999). More recent cosmological analyses, such as the Pantheon and Pantheon+ samples, have confirmed and refined these relations using thousands of SNe Ia (Scolnic et al. 2018; Brout et al. 2022).

In addition to these photometric diagnostics, spectroscopic diversity also provides crucial insight. Branch et al. (2006) defined four subgroups of SNe Ia based on the pseudo-equivalent widths (pEWs) of the Si II  $\lambda 6355$  and Si II  $\lambda 5972$  absorption lines near maximum light: core normal (CN) events, which exhibit intermediate line strengths and represent the archetypal normal population; broad line (BL) SNe Ia, distinguished by strong Si II  $\lambda 6355$  absorption and broader profiles indicative of higher ejecta velocities; cool (CL) SNe Ia, characterized by a high  $\lambda 5972/\lambda 6355$  ratio and generally subluminous behavior (including the 1991bg-like class); and shallow silicon (SS) SNe Ia, in which both Si II lines are weak, corresponding predominantly to the overluminous 1991T-like/1999aa-like subclass (see figure 1 of Branch et al. 2009 for representative spectra of each subtype). Wang et al. (2013) divided spectroscopically normal SNe Ia into two subgroups based on the Si II  $\lambda 6355$  velocity near maximum light: the normal velocity (NV;  $v \lesssim 11,800\text{kms}^{-1}$ ) and high velocity (HV;  $v \gtrsim 11,800\text{kms}^{-1}$ ) groups, which exhibit differences in color and host galaxy properties (see also Benetti et al. 2005). The Wang NV and HV groups vaguely overlap with the Branch CN and BL groups respectively.

These subclassification schemes are not merely empirical. CN events are broadly consistent with the standard Chandrasekhar-mass delayed-detonation model (Seitenzahl et al. 2013; Blondin et al. 2013), while BL/HV events are often interpreted as having more extended outer ejecta structures or stronger asymmetry, possibly linked to off-center ignition (Mazzali et al. 2005; Stehle et al. 2005; Maeda et al. 2010a) or the double-detonation model (Ogawa et al. 2023). CL events point to reduced  $^{56}\text{Ni}$  production and cooler ejecta (Nugent et al. 1995; Taubenberger et al. 2008; Dhawan et al. 2017). SS events, on the other hand, are associated with more extended burning or strong mixing (Ruiz-Lapuente et al. 1992; Sasdelli et al. 2014). Although no subtype can yet be tied to a unique progenitor channel or explosion mechanism, these patterns suggest that spectroscopic classifications carry physical significance, providing essential clues to the diversity of SNe Ia.

Efforts to link photometric and spectroscopic properties have focused primarily on peak-epoch observables. Benetti et al. (2005) showed that  $\Delta m_{15}(B)$ , defined as the difference in  $B$ -band magnitude between maximum light and 15 days afterward, correlates with the pEW ratio of the two Si II lines, and Hachinger et al. (2006) extended this to additional line ratios and the pEW of  $\lambda 5972$ , all of which correlate with peak luminosity. Folatelli et al. (2013), using 93 SNe Ia from the Carnegie Supernova Project, further quantified correlations between  $\Delta m_{15}(B)$ , pEWs, pEW ratios, and line velocities at maximum light. Colors of SNe Ia at peak are also found to have correlations with the pEW of Si II  $\lambda 6355$  Å, with lower velocities corresponding to bluer colors (Foley et al. 2011). More recent studies have begun to explore multi-epoch spectra; for instance, the time evolution of Si II, Ca II, O I, and S II features in early to near-peak spectra have been systematically analyzed (Zhao et al. 2015; Zhao et al. 2016; Zhao et al. 2021). However, comparisons that incorporate information from a wider range of epochs remain scarce, even though they promise a

more comprehensive view of SN composition and explosion history. Existing investigations have largely emphasized the evolution of specific line diagnostics within limited phase ranges, leaving open the broader connection between spectroscopic diversity and photometric behavior.

One compelling example is the secondary maximum seen in the  $I$ -band (and other NIR bands) 20–30 days after  $B$ -band peak. Kasen (2006) demonstrated that, as the ejecta cools to  $\sim 7000$  K, iron-group elements (IGEs) recombine and an inward-receding recombination front enhances  $I$ -band emissivity, producing the secondary peak. Variations in its timing and strength should reflect differences in physical properties such as  $^{56}\text{Ni}$  mass, mixing, and the synthesis of stable iron. On the observational side, Jack et al. (2015) identified a blended Fe II spectral feature around  $7,500$  Å in SN 2014J coinciding with the onset of the secondary maximum, providing empirical support for the theoretical mechanism. Observations have revealed diversity of this phase as well. Takanashi et al. (2008), hereafter TAK08, made  $UBVRI$  average light curves from 122 nearby SNe Ia and found that diversity was seen in the  $I$ -band secondary maximum, and that most of the outliers had peculiar spectroscopic properties. More recently, Deckers et al. (2025) analyzed nearly 900 SNe Ia from the Zwicky Transient Facility (ZTF) DR2 sample and statistically found correlations between the timing and strength of the  $r$ -band secondary maximum and  $\Delta m_{15}(g)$ . In the  $i$ -band, the timing showed a similar correlation, whereas the strength exhibited a larger scatter. While their study provided valuable empirical relations based purely on photometry, the underlying physical mechanism remains unclear. Some studies have found that some CL SNe Ia lack a distinct secondary maximum, which is thought to be due to low temperatures (Turatto et al. 1996; Dhawan et al. 2017). The secondary maxima of HV SNe Ia have also been found to show different behaviors from NV SNe Ia. Burgaz et al. (2021) found that HV SNe Ia have a larger scatter in magnitude and being brighter on average, and linked the luminosity difference to the distribution of  $^{56}\text{Ni}$  in the ejecta; that HV may have an ejecta structure with more  $^{56}\text{Ni}$  spread out in the outer regions. These results emphasize the need to link photometry and spectroscopy at various phases in their evolution.

In this work, we construct average  $UBVRI$  light curves for each Branch subtype to investigate how photometric evolution differs among spectroscopic classes. We then combine these light curve templates with spectral diagnostics to explore the underlying physical drivers of SN Ia diversity beyond maximum light. Section 2 describes our data sample and processing; section 3 details the creation of mean light curves; section 4 presents fitting results and the average light curves; and section 5 discusses the implications for progenitor systems and explosion physics.

## 2 Data

### 2.1 Archival data

The optical light curves of SNe Ia used in this study were obtained from two archival sources: the dataset compiled by TAK08, and data from the Carnegie Supernova Project (CSP; Krisciunas et al. 2017). TAK08 assembled their sample as Johnson-Cousins  $UBVRI$ -band (Bessell 1990) light curves from various papers (primarily Jha et al. 2006). In addition to the original TAK08 compilation, we incorporated several SNe Ia from the literature (SN 1990N, SN 1997cn, SN 1998aq, SN 1998bp, SN 1999by, SN 2002er, and SN 2003du). Because these objects were also ob-

served in the same *UBVRI* photometric system, we treat them as part of the TAK08 sample throughout this work. CSP data were acquired as *uBVri* system photometry (Stritzinger et al. 2011) using Swope 1-m telescope, and the Swope 2.5-m du Pont telescope at the Las Campanas Observatory (Krisciunas et al. 2017). From these datasets, we selected SNe Ia that had been classified into Branch subgroups in the literature (Branch et al. 2009; Folatelli et al. 2013), and had at least one data point in all five bands. All objects in our sample are at low redshift (figure 1). This yields a total sample of 109 SNe Ia, with 37 from the TAK08 sample and 72 from CSP. The number of SNe Ia used in this study is limited by the availability of public datasets that provide both multi-band light curves and high-quality spectra across multiple epochs. In practice, the combination of the TAK08 compilation and the Carnegie Supernova Project constitutes the principal open resources that meet these requirements, and our sample is therefore drawn from these surveys.

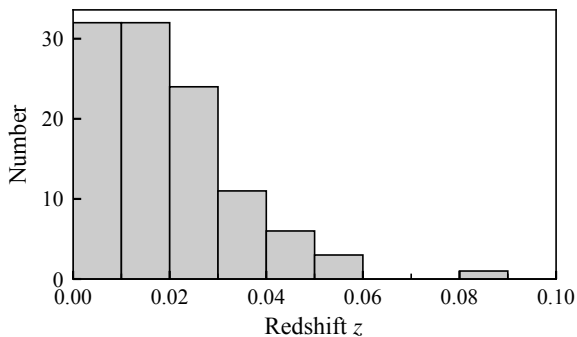


Fig. 1: Histogram of the redshift distribution of the SN Ia sample used in this work. Bins have a width of  $\Delta z = 0.01$ . Alt text: The x axis shows the redshift from 0.00 to 0.10. The y axis shows the number of supernovae, from 0 to 35.

We also examine optical spectroscopic properties to further explore the diversity among the Branch subgroups. The spectra employed in this analysis are taken from Blondin et al. (2012) and Folatelli et al. (2013). The values of pEWs are taken from Branch et al. 2009 for the TAK08 sample, and Folatelli et al. 2013 for the CSP sample.

Figure 2 displays the distribution of the pEWs of the two Si II absorption features for our sample. In this diagram, the different Branch subgroups are generally well separated. One notable exception is SN 1989B, which is classified as CL yet falls in the region predominantly occupied by BL SNe. Despite its weak Si II  $\lambda 5972$  feature, its overall spectral resemblance to CL justifies its assignment to that subgroup (see Branch et al. 2009). Table 1 summarizes the number of SNe in each Branch subgroup.

Table 1: The number of SNe Ia in each Branch subgroup.

Subgroup	Number	Poor fit*
Core normal (CN)	35	1
Broad line (BL)	28	2
Cool (CL)	26	13
Shallow silicon (SS)	20	0

\* The number of SNe Ia that yielded poor fits to the initial template (generic average light curves from TAK08), mostly due to peculiar *I*-band light curve shapes. Discussed in detail in section 4.4.

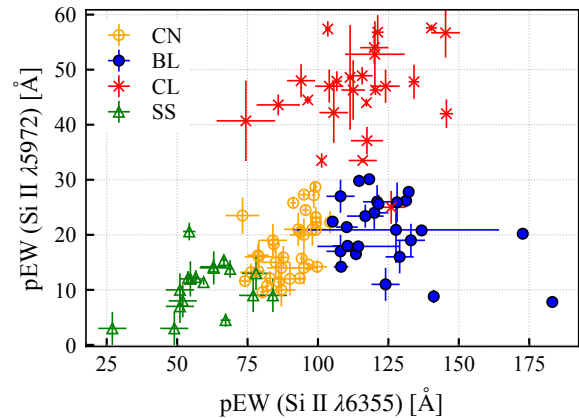


Fig. 2: Branch diagram showing pseudo-equivalent widths of Si II  $\lambda 6355$  versus Si II  $\lambda 5972$  for the SN Ia sample used in this work. Different subgroups are denoted by symbols: CN (orange open circles), BL (blue filled circles), CL (red crosses), and SS (open triangles). Values are from Branch et al. (2009) and Folatelli et al. (2013). Objects that lack measurements of either Si II line are not plotted here, but are retained for analyses that do not require pEWs. Alt text: A scatter plot diagram. The x axis shows the pseudo-equivalent width of the Si II absorption line at 6355 Angstroms, and the y axis shows those of the Si II line at 5972 Angstroms.

## 2.2 Light curve correction

As mentioned earlier, the light curves from TAK08 and CSP use different filter sets. The filter sets differ in wavelength range and transmission curves. Moreover, because SNe Ia at different redshifts have their observed photometry shifted to different wavelengths, it is necessary to apply a band correction to each data point prior to the construction of average light curves.

Our correction is based on the cross-filter K-correction method described by Kim et al. (1996). In brief, we compute synthetic magnitudes for a template spectrum in both the observed and rest-frame filter systems using the following equation:

$$K_{XY} = -2.5 \log_{10} \left[ \frac{1}{1+z} \cdot \frac{\int \lambda F_{\lambda} \left( \frac{\lambda}{1+z} \right) Y(\lambda) d\lambda}{\int \lambda F_{\lambda}(\lambda) X(\lambda) d\lambda} \times \frac{\int \lambda S_{\lambda}^X(\lambda) X(\lambda) d\lambda}{\int \lambda S_{\lambda}^Y(\lambda) Y(\lambda) d\lambda} \right], \quad (1)$$

where  $K_{XY}$  is the correction required to convert from the observed band  $Y$  to the rest-frame band  $X$ ,  $z$  is the redshift,  $F_{\lambda}(\lambda)$  is the flux density of the template spectrum,  $X(\lambda)$  and  $Y(\lambda)$  are the filter transmission functions, and  $S_{\lambda}^X(\lambda)$  and  $S_{\lambda}^Y(\lambda)$  represent the spectral energy distributions of the reference star used to define the zeropoints in each band.

The choice of spectral templates is motivated by their representative nature and widespread use. The Hsiao et al. (2007) spectra provide an empirical mean sequence of normal SNe Ia and are widely used for K-corrections and light curve modeling, making them appropriate for the CN and BL groups. Although high velocity features make BL spectra distinct from CN spectra, especially in the rising phase, dedicated BL templates are not currently available, and the Hsiao template provides a reasonable proxy, particularly as our analysis focuses on post-maximum phases where CN and BL spectra are broadly similar. For the CL and SS groups, the SN 1991bg-like and SN 1991T-like templates based on Nugent

et al. (2002)<sup>1</sup> are standard references that capture the distinctive spectral characteristics of these subclasses. Thus, the adopted set of templates reflects the most representative and publicly available resources for each Branch subgroup, ensuring consistency with previous work. Since the light curves from TAK08 are reported in the Vega magnitude system, we used a spectrum of Vega from the European Southern Observatory<sup>2</sup> to perform the conversion.

Because neither absolute magnitudes nor colors are used in this study, no correction for dust extinction was applied to avoid unnecessary uncertainty in the photometric values. Instead, we use  $B - V$  colors as values relative to the color at peak:

$$(B - V)_{\text{rel}}(t) = (B - V)(t) - (B - V)_{\text{peak}}. \quad (2)$$

For each light curve, the observed magnitude in band  $X$ ,  $m_X$ , is transformed to the rest-frame apparent magnitude in band  $Y$ ,  $m_Y$ , via

$$m_Y = m_X + K_{XY}. \quad (3)$$

### 3 Method

We construct average light curves for each Branch subgroup in two main steps: (1) fitting individual SN Ia light curves to a set of templates using a "multi-band stretch method", and (2) averaging the fitted light curves in each subgroup. This approach enables us to separate the effects of stretch, which is a well-studied parameter, from other potential light curve shape properties, and study the intrinsic diversity of SN Ia light curves comprehensively. Each of the following subsections details a part of the process.

#### 3.1 Light curve fitting

In our first step, we fit the light curve data to a set of template light curves with a multi-band stretch method described in TAK08. In this method, each photometric band is allowed its own stretch parameter, thereby providing a better overall fit and permitting the investigation of band-specific properties. We adopted the  $UBVRI$  average light curves from TAK08 as our initial template. This is a generic light curve made from SNe Ia of different subtypes altogether.

For each SN Ia, we determine a total of 11 parameters: the time of B-band maximum light, denoted as  $t_{B,\text{peak}}$ ; the stretch factors for each photometric band, represented as  $s_Y$ ; and the peak magnitudes for each band, indicated by  $m_Y$ , for  $Y = \{U, B, V, R, I\}$ .

The observed light curve data, consisting of points  $(t_{Y,i}, m_{Y,i} \pm \sigma_{Y,i})$ , are transformed into the template frame as follows:

$$\begin{cases} t'_{Y,i} = \frac{t_{Y,i} - t_{B,\text{peak}}}{s_Y(1+z)}, \\ m'_{Y,i} = m_{Y,i} - m_{Y,\text{peak}} + m_{\text{temp,peak}}. \end{cases} \quad (4)$$

Here,  $z$  denotes the redshift, and  $m_{\text{temp,peak}}$  is the peak magnitude of the template light curve.

For each band, we quantify the difference between the transformed data and the template by computing the weighted chi-square:

$$\chi_Y^2 = \sum_i \frac{[m_{\text{temp},Y}(t'_{Y,i}) - m'_{Y,i}]^2}{\sigma_{Y,i}^2 + \sigma_{\text{temp},Y}^2(t'_{Y,i})}. \quad (5)$$

For a fixed value of  $t_{B,\text{peak}}$ , we determine the candidate stretch and peak magnitude in each band,  $[s_Y^{\text{cand}}(t_{B,\text{peak}}), m_{Y,\text{peak}}^{\text{cand}}(t_{B,\text{peak}})]$ ,

that minimize  $\chi_Y^2$ . The overall chi-square is then obtained by summing over all bands:

$$\chi^2 = \sum_Y \chi_Y^2 \Big|_{s_Y = s_Y^{\text{cand}}(t_{B,\text{peak}}), m_{Y,\text{peak}} = m_{Y,\text{peak}}^{\text{cand}}(t_{B,\text{peak}})}. \quad (6)$$

The optimal set of parameters, denoted by  $(t_{B,\text{peak}}^{\text{fit}}, s_Y^{\text{fit}}, m_{Y,\text{peak}}^{\text{fit}})$ , is obtained by minimizing  $\chi^2$ . We denote the minimum value as  $\chi^2_{\text{min}}$  and define the reduced chi-square as  $\chi^2_{\text{red}} = \chi^2_{\text{min}}/\text{dof}$ , where "dof" represents the degrees of freedom.

Parameter uncertainties are estimated in the fitting to the initial template using a Markov Chain Monte Carlo (MCMC) approach implemented with the Python package `emcee` (Foreman-Mackey et al. 2013). An ensemble of 32 walkers was initialized near the optimal parameter estimates by adding small Gaussian perturbations. The sampler was run for 2000 iterations, with the first 500 iterations discarded as burn-in. The remaining samples were flattened across walkers, and the uncertainty for each parameter was computed as half the difference between the 84th and 16th percentiles of the posterior distribution.

Once the best-fit parameters are determined, each SN Ia light curve is transformed into the template frame (hereafter referred to as a "fit light curve").

#### 3.2 Making average light curves

For each Branch subgroup, we compile the fitted light curves to construct an average light curve. Initially, all fitted light curves for a given subtype are overlaid in a time versus magnitude frame to create a master light curve. Next, the data are binned along the time axis, and the weighted average magnitude in each bin is computed using the inverse square of the observational uncertainties as weights.

Because the temporal sampling density decreases substantially at later epochs, we adjust the bin widths as a function of time. For epochs earlier than 40 days after B-band maximum, we adopt a fixed bin width of 3 days. For later epochs, the bin widths are determined by a logarithmic function to ensure that the averaged magnitudes are not overly influenced by a few individual SNe. In addition, consecutive bins are allowed to overlap by half the width of the previous bin to promote smooth transitions in the average light curve.

As a result, we obtain stretch-free average  $UBVRI$  light curves for each subgroup. Since all light curves were initially fitted with a common template, the resulting averages still retain a strong dependence on that template. To reduce this bias and better represent the intrinsic properties of each Branch subgroup, we repeat the entire procedure iteratively. In each iteration, the average light curve from the previous cycle serves as the new fitting template. The process continues until the mean squared error (MSE) between the average light curves from successive iterations,  $\text{MSE}_i$ , falls below a threshold defined by the average uncertainty of the previous iteration,  $\bar{\sigma}_i$ :

$$\text{MSE}_i \leq \bar{\sigma}_i. \quad (7)$$

## 4 Results

### 4.1 Fitting results

The best fit parameters and uncertainties for all SNe Ia fit to the initial template are provided in appendix 1 (table 5). Hereafter, stretch is defined so that  $s = 1$  for all bands in the initial template.

<sup>1</sup> [https://c3.lbl.gov/nugent/nugent\\_templates.html](https://c3.lbl.gov/nugent/nugent_templates.html)

<sup>2</sup> <https://www.eso.org/sci/observing/tools/standards/spectra/hr7001.html>

In the main text, we focus on distribution-level trends and representative correlations.

Throughout this study, we distinguish between two definitions of phase. "Observed phase" refers to the epoch relative to  $B$ -band maximum without correction, while "stretch-corrected phase" refers to the time axis after dividing it by the fitted stretch factor. Unless otherwise noted, results comparing multiple subtypes (e.g., figures 5, 11) are presented in the stretch-corrected phase in order to remove the first-order effect of  $^{56}\text{Ni}$  mass.

We first inspect the distribution of the derived stretch parameters. Figure 3 shows the distribution of stretch values for well-fit SNe Ia ( $\chi_{\text{red}}^2 \leq 4$ ) in each subtype. Although the subtypes share overlapping ranges of stretch values, their averages differ (table 2). In all bands, average stretch values increase in the order of CL, BL, CN, and SS.

It is well established that CL SNe Ia tend to have small stretch values, while SS SNe Ia exhibit large ones (e.g., Folatelli et al. 2013). The distinction between CN and BL, however, has been less clear. Blondin et al. (2012) reported that BL events have a slightly steeper  $B$ -band decline rate ( $\Delta m_{15}(B)$ ) than CN, whereas Folatelli et al. (2013) found no significant difference. Our results provide new evidence by demonstrating that BL consistently shows smaller stretch than CN across all optical bands, not just in the  $B$ -band.

The stretch parameter represents the characteristic timescale of the light curve, which depends on the opacity, ejecta mass, and ejecta velocity (Arnett 1982). The amount of synthesized  $^{56}\text{Ni}$  affects the opacity and thus the diffusion timescale. Observationally, however, the ejecta velocity shows little or no correlation with stretch (Pan et al. 2024). This suggests that variations in stretch primarily reflect differences in the  $^{56}\text{Ni}$  and ejecta masses.

We then examined how the fitted stretch parameters in each band correlate with the pEWs of the Si II  $\lambda 5750$  and  $\lambda 6355$  absorption lines and their ratio. Three representative cases that compare  $V$ -band stretch to the pEWs are shown in figure 4. Across the full sample, light curves with larger stretch tend to have weaker Si II absorption. The pEW ratio of the two Si II lines also correlate with stretch. Similar results for the other bands and subtype-resolved correlation coefficients are presented in appendix 2 (figures 14–17; table 6). These results are consistent with previous work (e.g., Benetti et al. 2005; Folatelli et al. 2013), but this work further extends these correlations to other optical bands.

When divided by Branch subtype, however, these inverse stretch–pEW trends are not uniform. CN, BL, and CL retain robust anti-correlations with the Si II  $\lambda 5972$  feature in every band, whereas SS shows little to no relation, likely at least partially reflecting the difficulty of measuring weak Si II in SS. For the stronger Si II  $\lambda 6355$  line, only CN preserves a significant negative slope in  $B$ ,  $V$ ,  $R$ , and  $I$ ; BL weakens, and CL/SS are largely uncorrelated. Taking the pEW ratio,  $\text{pEW}(\text{Si II } \lambda 5972) / \text{pEW}(\text{Si II } \lambda 6355)$ , sharpens the stretch dependence for CL (reaching  $|\tau| \sim 0.8$ ), while SS remains uncorrelated. These systematic differences by Branch subclass show that stretch values correlate with different spectroscopic parameters across the subclasses. One alternative explanation is that, because each subclass spans only a limited range of stretch values, the correlations appear less pronounced when the groups are analyzed separately. Nevertheless, the difference between CN and BL remains noteworthy, since the widths of their stretch distributions are comparable.

## 4.2 Average light curves

Following the method described earlier, the template light curves for each Branch subtype were constructed by iteratively refining the fit until the residual difference between consecutive iterations converged below a critical threshold. Table 3 summarizes the number of iterations performed for each subtype and photometric band.

Figure 5 shows the resulting average light curves for each Branch subtype across the  $U$ ,  $B$ ,  $V$ ,  $R$ , and  $I$  bands. In these plots, the peak magnitudes have been normalized to 0.0 mag to facilitate comparison between subtypes. To illustrate the data coverage and dispersion, all individual light curves used to construct these averages are overplotted in appendix 3 (figure 18).

Notably, in the  $I$ -band, the BL, CL, and SS light curves exhibit a more prominent secondary maximum relative to the primary peak compared to the CN light curve (figure 6). The pronounced secondary maximum seen in SS objects is consistent with theoretical predictions that more luminous SNe Ia exhibit stronger secondary maxima (e.g., Kasen 2006). The trend in CL is noteworthy given its departure from the conventional view of CL (91bg-like) events, which are generally understood to display weak or absent secondary peaks in the NIR. Note that CL SNe Ia with no secondary peaks have been excluded from the sample for making average light curves because of their poor fits; these results are solely from CL SNe Ia that have secondary peaks.

The differences between CN and BL are newly found as well. While previous work (e.g., Burgaz et al. 2021) identified an excess in the  $I$ -band around the secondary peak in HV SNe Ia, this finding has not been broken down by the Branch subclass, and by a sample size of this study. Thus, our findings that BL SNe Ia (which often overlap with the HV category) show enhanced  $I$ -band secondary maxima represents a novel contribution to the characterization of subclass diversity.

Interestingly, we also find that the CL light curve shows a more gradual decline after about 50 days past  $B$ -band maximum. While previous studies have emphasized their rapid post-maximum evolution (e.g. Taubenberger et al. 2008), the relative shallowness of their late-time decline has not, to our knowledge, been reported before. In the  $R$ -band, the CL subgroup also deviates from the other groups by displaying a slower decline after the first peak and an almost absent plateau.

## 4.3 Color curves

The evolution of SN colors reflects underlying physical properties, such as the temperature of the ejecta and the reprocessing of blue light into longer wavelengths by iron-group element lines. To study this behavior, we used the average light curves to derive average  $B - V$  color curves for each subtype (figure 7). In order to compute  $B - V$  consistently, we placed the mean  $B$  and  $V$ -band light curves on the observed phase using their corresponding average stretch factors. This procedure placed the two bands on the same observed time axis, ensuring that their relative timescales were accurately reproduced. The color curves have been normalized so  $B - V = 0$  at  $B$ -band maximum; hereafter, we denote color as  $(B - V)_{\text{rel}}$ , the value relative to the peak color.

All subtypes exhibit an initial reddening phase up to  $\sim 20$ -30 days past  $B$ -band maximum, followed by a gradual return toward bluer colors. Notably, the CL subtype reaches the maximum peak color ( $\sim 1.18$  mag) most rapidly, while the SS subtype evolves more slowly and peaks at a slightly lower  $(B - V)_{\text{rel}}$  value ( $\sim 1.08$  mag). CN and BL have similar peak colors to SS, but their timings vary. These differences suggest systematic variations in

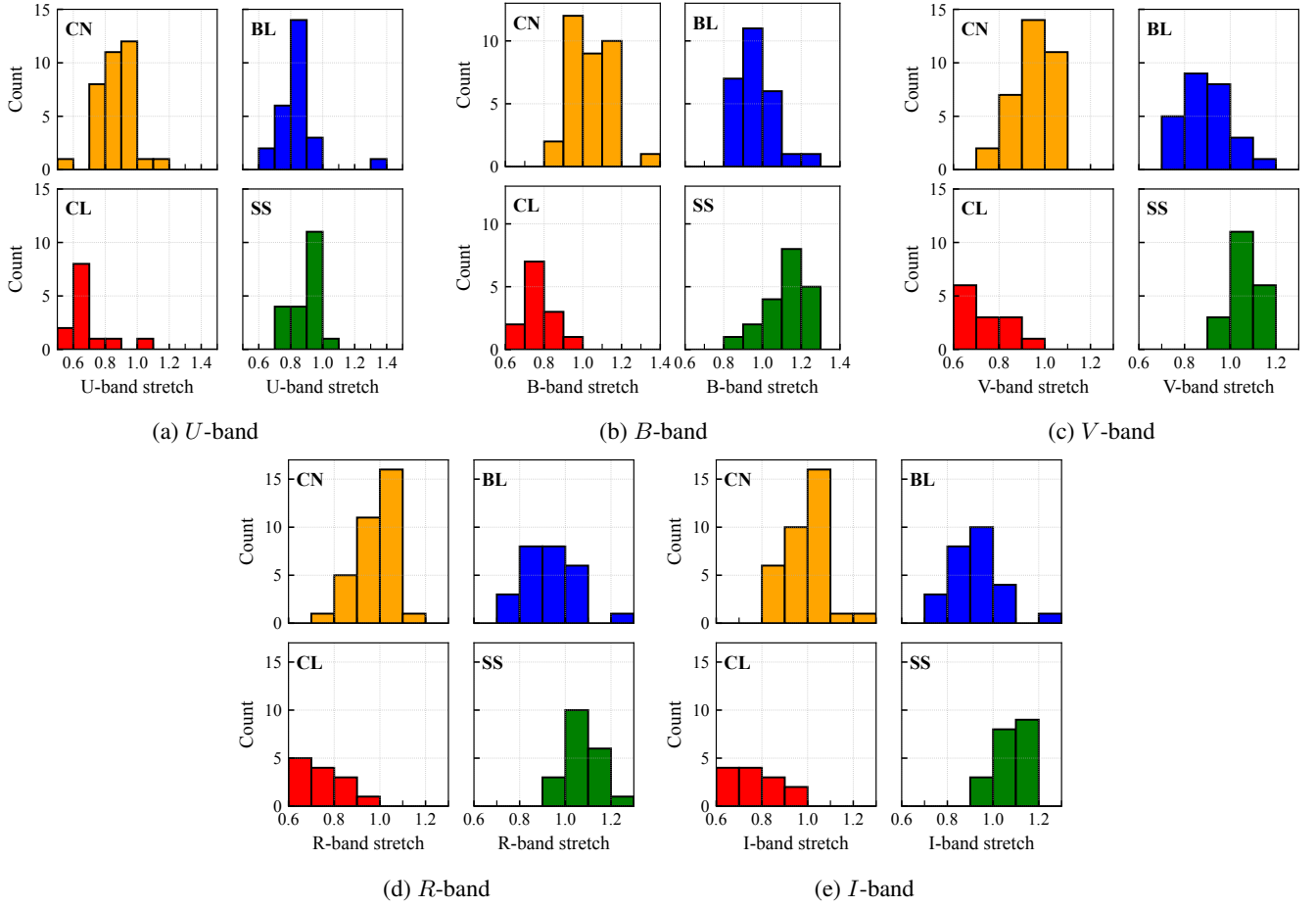


Fig. 3: Histograms of stretch distributions for each Branch subtype. Stretch values are defined so that  $s = 1$  for the initial template. Alt text: An ensemble of histograms. There are five parts of the figure, corresponding to UBVR I bands. Each part is consisted of four panels, corresponding to the Branch subgroups. Each panel has an x axis showing the stretch value in that band, and the y axis showing the number of supernovae.

Table 2: Weighted mean  $\pm 1\sigma$  of stretch parameters for each Branch subtype.

Subgroup	$\overline{s_U^{\text{fit}}}$	$\overline{s_B^{\text{fit}}}$	$\overline{s_V^{\text{fit}}}$	$\overline{s_R^{\text{fit}}}$	$\overline{s_I^{\text{fit}}}$
CN	$0.847 \pm 0.084$	$1.012 \pm 0.091$	$0.928 \pm 0.069$	$0.958 \pm 0.097$	$0.949 \pm 0.093$
BL	$0.834 \pm 0.074$	$0.951 \pm 0.076$	$0.863 \pm 0.088$	$0.905 \pm 0.099$	$0.885 \pm 0.088$
CL	$0.660 \pm 0.051$	$0.802 \pm 0.073$	$0.740 \pm 0.085$	$0.740 \pm 0.078$	$0.771 \pm 0.079$
SS	$0.847 \pm 0.095$	$1.146 \pm 0.063$	$1.059 \pm 0.046$	$1.078 \pm 0.054$	$1.091 \pm 0.053$

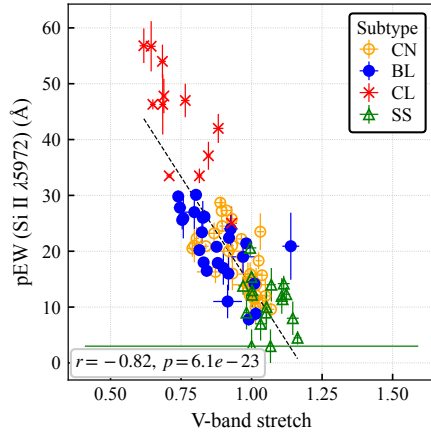
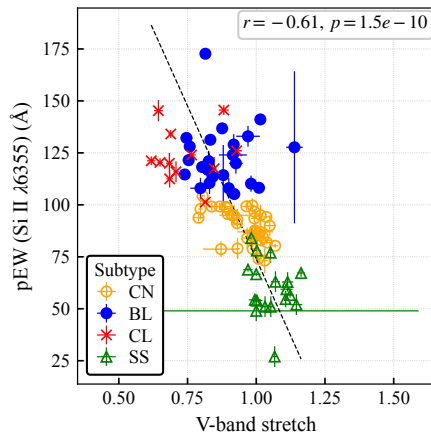
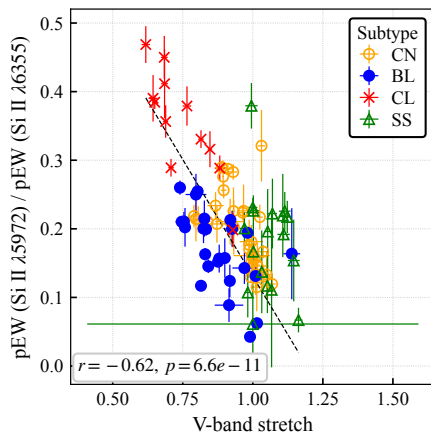
(a)  $V$ -band stretch vs. pEW (Si II  $\lambda 5972$ )(b)  $V$ -band stretch vs. pEW (Si II  $\lambda 6355$ )(c)  $V$ -band stretch vs. pEW ratio of Si II  $\lambda 5972$  and  $\lambda 6355$ 

Fig. 4: Correlation between  $V$ -band stretch and the pEW of (a) Si II  $\lambda 5972$ , (b) Si II  $\lambda 6355$ , and (c) their ratio. Symbols follow the same convention as in figure 2. The dashed line in each panel shows the best fit linear relation obtained with orthogonal distance regression. The Pearson coefficient  $r$  and  $p$ -value are also shown. Alt text: A figure consisting of three panels. All panels have  $V$ -band stretch as the x axis. The y axes show the pseudo-equivalent widths of the Si II line at 6355 Angstroms, the Si II line at 5972 Angstroms, and the ratio of the two lines, for each panel.

Table 3: The number of samples (iterations) used to make the average light curve for each subtype and band.

Subgroup	$U$ -band	$B$ -band	$V$ -band	$R$ -band	$I$ -band
CN	33 (2)	33 (2)	33 (2)	33 (2)	33 (2)
BL	23 (2)	23 (2)	23 (2)	23 (2)	23 (2)
CL	15 (7)	13 (2)	13 (2)	11 (9)	16 (3)
SS	17 (2)	17 (2)	17 (2)	16 (4)	17 (2)

fluorescence among the subtypes. In table 4 we summarize the peak  $(B - V)_{\text{rel}}$  values and epochs for each subtype, estimated by smoothing the color curves.

Table 4: Peak epochs and amplitudes of the  $B - V$  color curves for each Branch subtype. Values were measured from Savitzky-Golay-smoothed profiles (window length= 51 days, polynomial order= 3).

Subtype	Epoch of $(B - V)_{\text{rel,max}}$	$(B - V)_{\text{rel,max}}$
CN	$32.2 \pm 1.9$	$1.097 \pm 0.034$
BL	$26.1 \pm 1.4$	$1.106 \pm 0.029$
CL	$19.5 \pm 1.3$	$1.239 \pm 0.040$
SS	$43.9 \pm 6.2$	$1.054 \pm 0.070$

It is worth noting that the SS color curve evolves much more slowly after maximum, nearly forming a plateau, whereas the other subgroups become bluer at broadly similar rates. Between phases +30 and +90 d, the  $B - V$  colors of SNe Ia is known to be approximately linear (the Lira relation; Lira 1995; Phillips 1999). More recent work indicates that the Lira-phase slope depends on light-curve shape (e.g., color stretch  $s_{BV}$ ; Burns et al. 2014). These results may expand the known diversity in  $B - V$  evolution, with SS occupying the shallow slope end of the distribution.

Overall, the ordering of peak color timing largely follows the known stretch/ $\Delta m_{15}(B)$  sequence: CL events redden and peak earliest, BL and CN show intermediate behavior, and SS evolves most slowly. This consistency suggests that the diversity in color evolution is closely linked to the width–luminosity relation and ultimately to the amount of synthesized  $^{56}\text{Ni}$  and its distribution.

#### 4.4 SNe Ia with poor fits

We define "poor fit SNe Ia" as objects with a reduced chi-square value of  $\chi_{\text{red}}^2 \geq 4$  in the first iteration when fitted to the initial template. The number of poor fit samples in each Branch subgroup is presented in table 1.

Most of the poor fits arise from the absence of a clear secondary maximum in the  $I$ -band light curve, the lack of a plateau in the  $R$ -band light curve, or both (an example is shown in figure 8). This behavior is particularly evident in the CL subgroup. In these subluminous events, the ejecta cools more rapidly after maximum, and the photospheric temperature reaches  $\sim 7,000$  K earlier than normal SNe Ia. At this temperature, the secondary maximum would usually appear, but in CL events it occurs so early that it merges with the primary peak. The resulting overlap of the first and second peaks causes deviations from the expected template shape and leads to higher  $\chi_{\text{red}}^2$  values. In addition, some SNe Ia exhibit poor fits due to insufficient data around the peak or in the  $R/I$  bands, where the light curve morphology is more complex than in other bands.

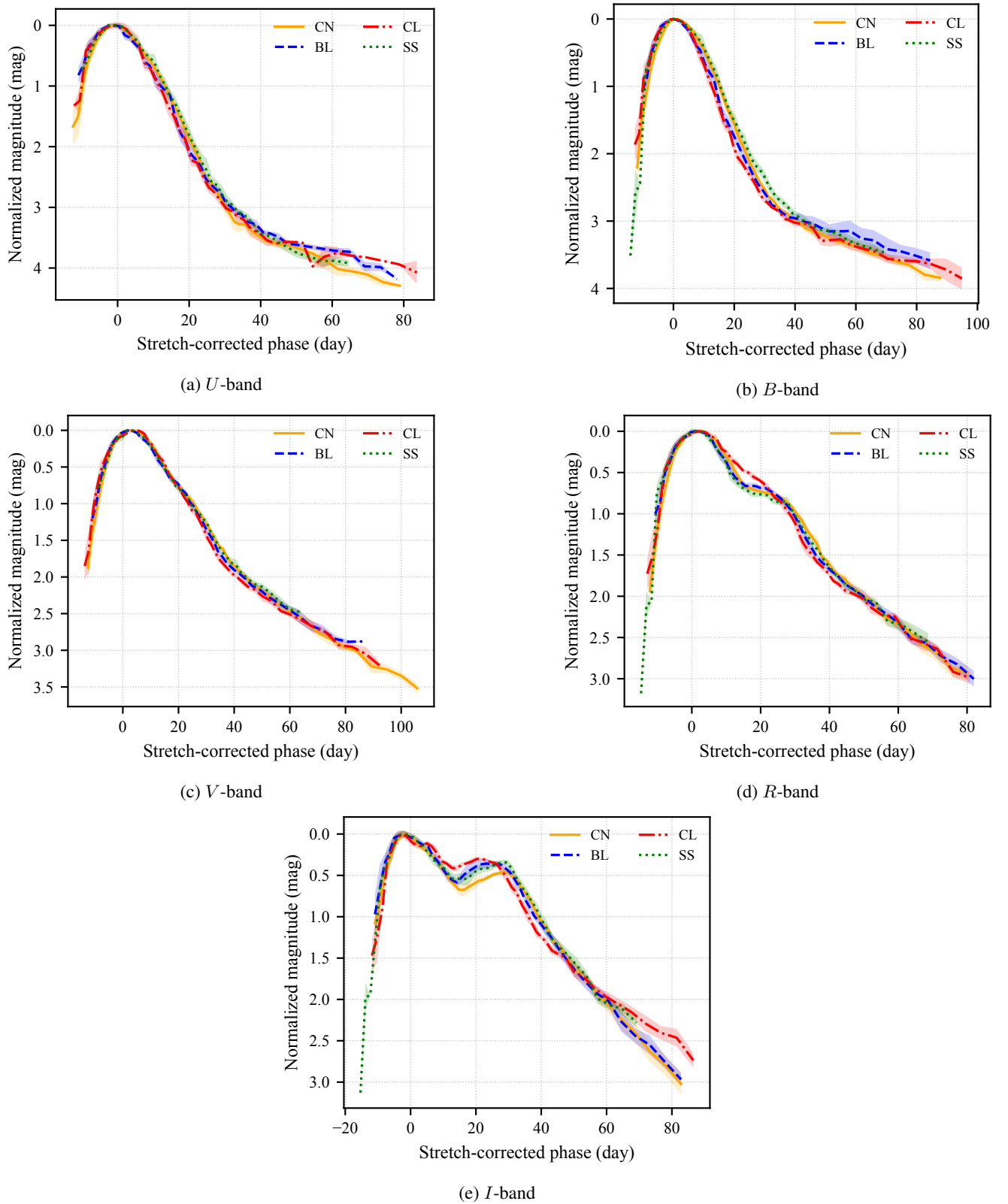


Fig. 5: Average light curves of each Branch subtype in the *U*, *B*, *V*, *R*, and *I*-bands. Epochs are in stretch-corrected phases relative to the *B*-band maximum. Peak magnitudes are normalized to 0.0 mag. Colors and line styles correspond to Branch subtypes: CN (orange solid), BL (blue dashed), CL (red dash-dotted), and SS (green dotted). Shaded regions indicate  $1\sigma$  dispersions of the sample in each bin. Alt text: The figure consists of five panels corresponding to the UBVRI bands. Each panel shows average light curves of the four Branch subgroups, with stretch-corrected phase on the x axis and normalized magnitude on the y axis.

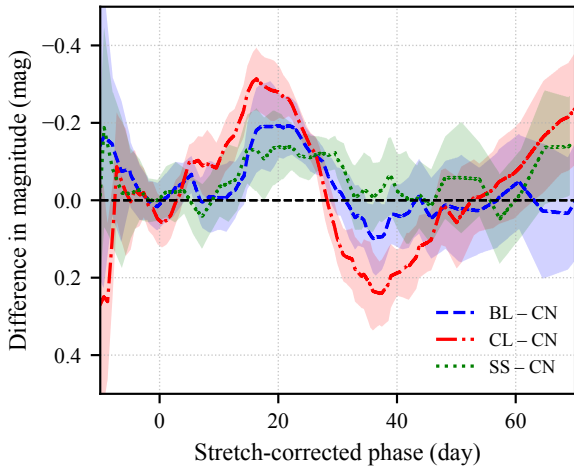


Fig. 6: Residuals of the  $I$ -band average light curves of BL, CL, and SS subtypes relative to CN, shown as a function of stretch-corrected phase. Shaded regions indicate the  $1\sigma$  uncertainties propagated from the dispersions of the two subtypes. Alt text: The x axis shows the stretch-corrected phase, and the y axis shows the difference in magnitude between core normal supernovae and those from the other groups.

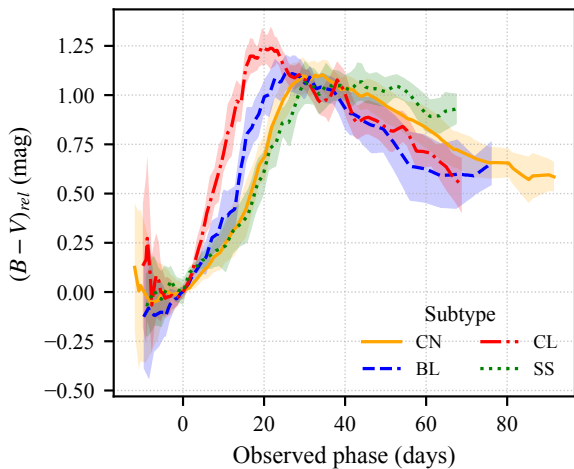


Fig. 7:  $(B - V)_{rel}$  color curves of SNe Ia, grouped by Branch subtype, shown as a function of observed phase relative to  $B$ -band maximum. Curves are normalized to  $(B - V) = 0$  at maximum light. Alt text: A line graph with the x axis as observed phase, and the y-axis as the color relative to B-band maximum.

## 5 Discussion

The pronounced diversity of  $I$ -band light curves among SNe Ia, especially in the secondary maximum and the late-time decline, provides a powerful diagnostic of explosion physics. Here, we first demonstrate that the Fe II line evolution, rather than continuum or Ca II features, drives the diversity of the secondary maximum. We then show how the late-time  $I$ -band slope can serve as a photometric indicator of the CL subclass.

### 5.1 Diversity of the $I$ -band secondary maximum

Theoretical work attributes the  $I$ -band secondary maximum to iron recombination as the ejecta cools to  $\sim 7,000$  K, causing Fe II lines

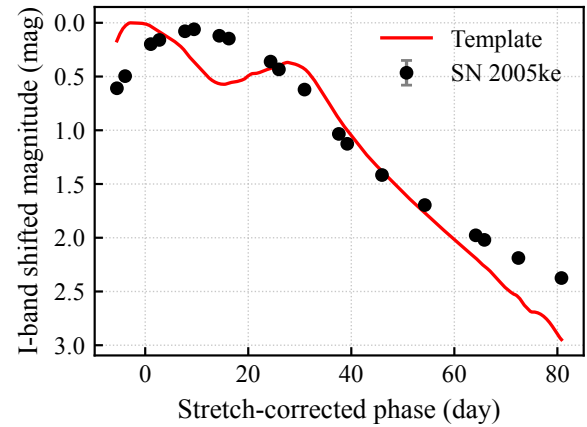


Fig. 8: The fit  $I$ -band light curve of CL SN Ia SN 2005ke (black circles) with the initial TAK08 template (red solid curve). Most of the poor fit SNe Ia have peculiar  $I$ -band light curves with only one peak like this SN, resulting in  $\chi^2_{red} \geq 4$ . Alt text: A graph. The x axis shows stretch-corrected phase, and the y axis shows  $I$ -band shifted magnitude.

to emerge (Kasen 2006; Jack et al. 2015). To test this idea, we took the CSP spectrum data in the  $i$ -band wavelength window (6,960–8,340 Å, corresponding to  $\geq 40\%$  of the maximum transmittance) and divided them into three regions: (1) a Fe II region (7,300–8,000 Å), (2) a non-Fe II region including the adjacent continuum plus Ca II absorption (6,960–7,300 Å and 8,000–8,340 Å), and (3) a complementary redward Ca II emission region (8,340–8,870 Å). After normalizing each spectrum to its interpolated photometric magnitude, we generated synthetic light curves by integrating flux within these regions. We do not use spectra from the TAK08 sample, as they do not cover the full  $I$ -band wavelength range.

Figure 9 presents these wavelength divisions alongside their corresponding synthetic light curves. The results show that the Fe II region dominates the secondary maximum, whereas the non-Fe II and Ca II region does not show a strong bump; consequently, Ca II emission features are excluded from further discussion of subclass-dependent spectral diversity. Moreover, the observation that all subclasses exhibit similar color at the time of the secondary peak (figure 10), implies that the emergence of Fe II features occurs under comparable thermal conditions, providing statistical support for models that link the  $I$ -band secondary maximum to recombination of iron-group elements. This further indicates that the recession of the photosphere is coupled with the iron recombination front, linking the observed color evolution directly to the transition from photosphere-powered to line-powered luminosity. This further indicates that the recession of the photosphere is coupled with the iron recombination front. These results are consistent with the theoretical prediction of Kasen (2006), and the spectroscopic evidence found by Jack et al. (2015) and Deckers et al. (2025), all of which point to Fe II emission as the dominant origin of the secondary maximum.

Subtype-specific Fe II light curves are presented in figure 11. Note that these light curves (as well as the light curves in figure 9) have been corrected for stretch. The diversity seen in this figure is slightly different from the overall  $I$ -band light curves (figure 5); here, the amplitudes of the secondary maximum of CN, BL, and SS do not change greatly. This suggests that although the non-Fe II regions do not contribute to the secondary maximum significantly, changes in its light curves like the slope could change the strength

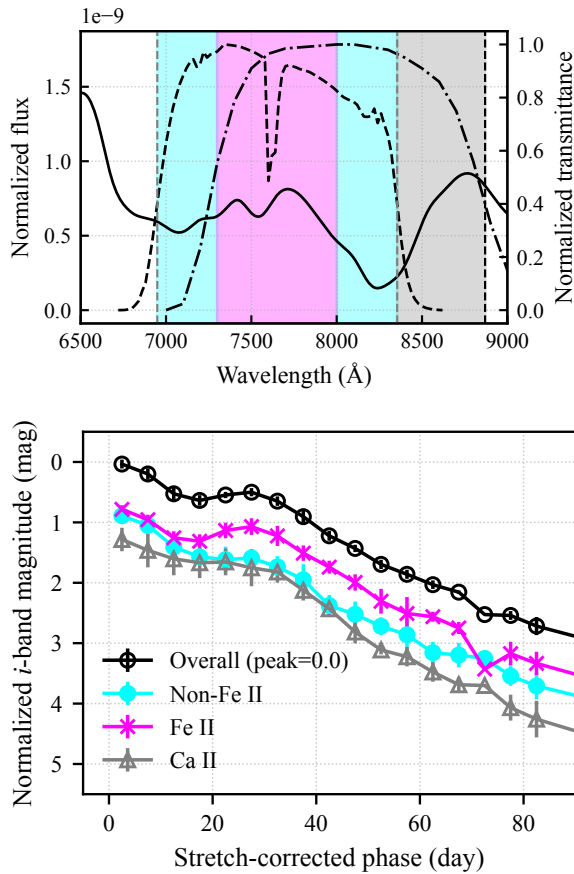


Fig. 9: The top panel shows the wavelength ranges used for the decomposition of the  $i/I$ -band. The black solid line shows the Hsiao spectral template at +28 days, while the black dashed and dot-dashed lines denote the CSP  $i$  and Bessell  $I$  filter transmission curves, respectively. The magenta band marks the Fe II region (7,300–8,000  $\text{\AA}$ ), the gray band indicates the Ca II region (8,340–8,870  $\text{\AA}$ ), and the cyan bands correspond to the non-Fe II contributions (6,960–7,300  $\text{\AA}$  and 8,000–8,340  $\text{\AA}$ ). Vertical dashed lines mark the 40% transmittance thresholds of each filter. The bottom panel presents the corresponding synthetic light curves in stretch-corrected phase, normalized to zero at peak. Shown are the overall light curve (black open circles), the non-Fe II contribution (cyan filled circles), the Fe II contribution (magenta crosses), and the Ca II contribution (gray open triangles). Alt text: In the top panel, the x axis shows wavelength. The y axis is used for two quantities, normalized flux and transmittance. In the bottom panel, the x axis shows stretch-corrected phase, and the y axis shows the normalized  $i$ -band magnitude.

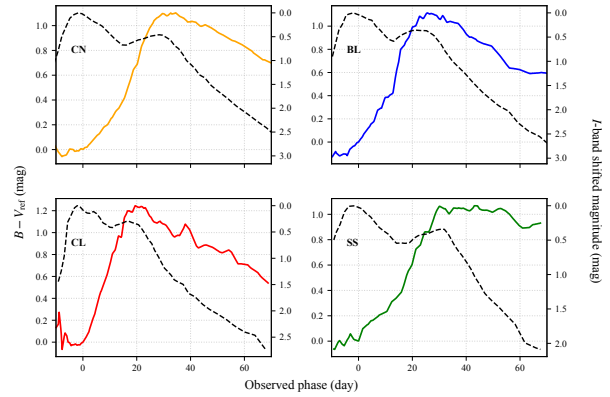


Fig. 10: Normalized synthetic light curves for each Branch subtype, comparing the overall  $i$ -band magnitude (black dashed line) to the  $(B - V)_{\text{rel}}$  color evolution (solid colored line) on a common observed phase axis. Alt text: The figure consists of four panels, each corresponding to different Branch subgroups. In each panel, the x axis shows the observed phase. The y axis is used for two quantities, the  $B - V$  colors related to  $B$ -band maximum, and shifted  $i$ -band magnitudes.

of the bump.

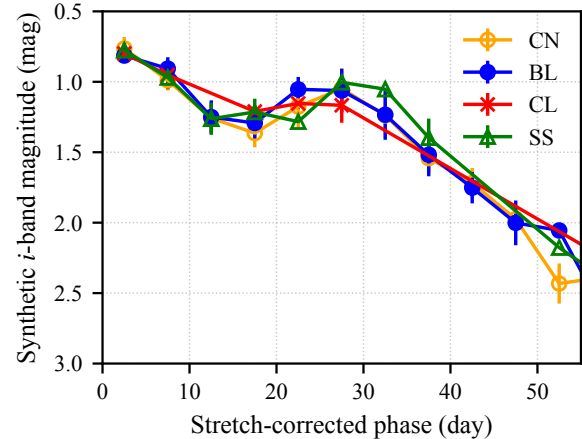


Fig. 11: Subtype-resolved synthetic light curves in stretched-corrected phases computed solely within the Fe II region (7,150–8,000  $\text{\AA}$ ). Alt text: A line graph. The x axis shows stretch-corrected phase, and the y axis shows normalized  $i$ -band magnitude.

Hereafter, we focus on the diversity of the Fe II region light curves, which had the greatest contribution to the secondary maximum. The amplitude still shows some variety, with CL having a weaker secondary maximum than the other subgroups. However, it is rather the timing that varies for different subgroups, with CL and BL having earlier peaks than CN and SS. The significance of this trend can be further confirmed by collecting more spectra around the secondary maximum, because figure 11 is binned by 5 days due to the limited number of spectra.

## 5.2 Interpretations from theoretical models

Kasen (2006) performed radiative transfer simulations for certain ejecta structures to calculate the effects of different physical pa-

rameters to the behavior of the secondary maximum in NIR bands, including the I-band. The parameters discussed were the degree of  $^{56}\text{Ni}$  mixing,  $^{56}\text{Ni}$  mass, and the amount of stable iron elements. Here, we discuss each parameter and its possible effect on our results.

Variation in  $^{56}\text{Ni}$  mass primarily affects the peak luminosity and the overall time scale of the light curve. Observationally, Folatelli et al. (2013) reported that the mean peak absolute magnitudes follow the sequence  $\text{CL} < \text{BL} < \text{CN} < \text{SS}$ . Since the luminosity of SNe Ia is proportional to the amount of  $^{56}\text{Ni}$ , this suggests that the  $^{56}\text{Ni}$  mass systematically increases from CL to SS. The overall timescale, represented by the stretch parameter, also follows the same order ( $\text{CL} < \text{BL} < \text{CN} < \text{SS}$ ), consistent with the interpretation from peak luminosity diversity. However, as mentioned in section 4.1, the stretch parameter is not solely determined by  $^{56}\text{Ni}$  mass, as it also depends on the total ejecta mass through the diffusion timescale (Arnett 1982). Therefore, while the correlation between peak luminosity and stretch implies a major influence from  $^{56}\text{Ni}$ , the role of the ejecta mass cannot be ignored. The effects of these two masses can be distinguished in future work by directly measuring  $^{56}\text{Ni}$  mass from nebular lines (Childress et al. 2015; Mazzali et al. 2015). A larger  $^{56}\text{Ni}$  mass tends to delay the secondary maximum and enhance its strength, which could in principle account for part of the observed diversity.

In this study, we use stretch-normalized light curves in our discussion (figures 5 and 11), which is expected to largely remove the first-order effect of  $^{56}\text{Ni}$  mass. If the timing of the secondary maximum were insensitive to ejecta mass, such normalization could mix ejecta mass diversity into the stretch-corrected phase. However, several observational studies suggest that the secondary maximum is related to the ejecta mass. Papadogiannakis et al. (2019) found that SNe Ia with longer transparency timescales, which serve as an observational proxy for larger ejecta masses, tend to show later secondary maxima. Furthermore, Dhawan et al. (2015) reported that the timing of the secondary maximum in the near-infrared correlates with the  $B$ -band decline rate (i.e. stretch), which reflects variations in both  $^{56}\text{Ni}$  and ejecta mass. Since  $B$ -band light curves become strikingly uniform after stretch correction, it is likely that this procedure effectively removes the diversity arising from both  $^{56}\text{Ni}$  and ejecta masses. Based on these considerations, we assume that the stretch normalization approximately compensates for the combined effects of  $^{56}\text{Ni}$  and ejecta mass for the  $I$ -band, and we proceed with this interpretation in the following discussion.

The residual diversity after correcting for stretch manifests almost exclusively in the timing of the secondary maximum, and cannot be explained by  $^{56}\text{Ni}$  mass and ejecta mass alone. This indicates that an additional parameter must be invoked that alters the timing without significantly changing the amplitude. Nevertheless, the influence of  $^{56}\text{Ni}$  mass and ejecta mass cannot be regarded as completely absorbed by stretch: for instance, brighter SS events may retain higher temperatures that could delay the onset of recombination. Although the stretch-corrected color curves are broadly consistent across subtypes, implying similar temperature evolutions, we do not entirely rule out a residual effect of these two masses.

One leading candidate that can explain the remaining diversity is the mass of stable iron group elements (IGEs) synthesized in the explosion. Stable IGEs do not contribute to the overall luminosity of the supernova, but they change the radius of the iron-rich core, hastening or delaying the secondary maximum. In Kasen (2006), the amount of stable IGEs synthesized by electron capture has an

effect of changing the timing of the secondary maximum without changing the brightness, which is the trend seen in our results. In figure 11, the BL and CL subgroups have earlier secondary peaks than the CN and SS subgroups, which would imply that more stable IGEs relative to  $^{56}\text{Ni}$  were synthesized during the explosion in the former groups. Stable IGEs can also be synthesized when the metallicity of the WD is high, but this has an effect of changing the secondary maximum amplitude as well, which is not consistent with our results. Nevertheless, analysis with NIR light curves may be able to distinguish these parameters in future work.

Mixing of  $^{56}\text{Ni}$  is also capable of changing the timing and brightness of the secondary maximum. However, in the case of the  $I$ -band, the effect shifts the primary peak along with the secondary peak, weakening the relative variations (see figure 9 of Kasen 2006). Therefore, we concluded that stable IGEs is likely to have a stronger effect. However, it is worth noting that when assuming a completely homogenized composition structure, the first and second peaks become blended together to form a single late peak, which is consistent with some CL SNe Ia which did not fit well to the template. Mixing cannot be completely neglected, and other diagnostics are required to robustly distinguish between the two effects in future work. One candidate could be the shape of the early light curves, as it is predicted that SNe Ia with different  $^{56}\text{Ni}$  distribution have different early light curve behavior (Magee et al. 2018).

Kasen (2006) also found that the Ca II line can affect the secondary maximum in the  $I$ -band, depending on assumptions of radiative transfer: pure scattering and pure absorption. It was concluded that if calcium lines were from pure scattering, it would have only a modest effect on the secondary maximum. On the other hand, if pure absorption was assumed, the luminosity would change substantially. In this study, we have shown that the amplitude of the secondary maximum does not vary drastically (especially after the effect of  $^{56}\text{Ni}$  mass is corrected for), and that Ca II does not have a significant contribution to the bump (figure 9), so this effect can be neglected. Observations are more consistent with the pure scattering case.

### 5.3 Physical differences between the Branch subgroups

Previous studies have suggested that the CL, CN, and SS subtypes may form a continuous sequence, broadly consistent with the stretch-magnitude relation and largely driven by differences in the amount of synthesized  $^{56}\text{Ni}$  (Nugent et al. 1995; Branch et al. 2006).

Our results indicate that the timing of the secondary maximum (after correcting for stretch) is particularly sensitive to the amount of stable IGEs, making this parameter a strong candidate for driving the observed diversity. CL and BL events show earlier secondary maxima than CN and SS, implying that they produced larger amounts of stable IGEs. Given that the  $^{56}\text{Ni}$  mass increases in the order of CL, BL, CN, SS, we see an anti-correlation between stable IGE mass and  $^{56}\text{Ni}$  mass; subgroups that synthesize more  $^{56}\text{Ni}$  tend to produce fewer stable IGEs.

This trend is broadly consistent with the near- $M_{\text{Ch}}$  delayed-detonation scenario, where high-luminosity explosions with more  $^{56}\text{Ni}$  tend to produce less IGEs due to less efficient electron capture (Krueger et al. 2010; Seitenzahl et al. 2013). On the other hand, the sub- $M_{\text{Ch}}$  double-detonation scenario predicts the opposite trend: both  $^{56}\text{Ni}$  and stable IGEs (e.g.,  $^{58}\text{Ni}$ ,  $^{57}\text{Fe}$ ) increase with the progenitor mass, leading to a positive correlation between the yields of

these elements (Woosley & Kasen 2011). Therefore, the observed sequence from CL to SS is naturally explained within the framework of the near- $M_{\text{Ch}}$  delayed detonation scenario, while it is inconsistent with the expectations of the sub- $M_{\text{Ch}}$  double-detonation scenario.

Within this delayed-detonation sequence, BL events may represent an intermediate case, with the amount of stable IGE between CL and CN. However, some studies have interpreted the spectroscopic differences between BL and CN as reflecting differences in ejecta structure, such as viewing angles in an asymmetric explosion (Maeda et al. 2010a) or outward mixing of intermediate mass and iron group elements (Mazzali et al. 2005; Stehle et al. 2005). In such scenarios, the relatively early secondary maximum could arise from a shallower distribution of radioactive material in the ejecta. BL events might even originate from different explosion mechanisms altogether, such as the sub- $M_{\text{Ch}}$  double-detonation scenario, rather than representing an intermediate state within a continuous near- $M_{\text{Ch}}$  sequence. This would provide an alternative explanation for the smaller stretch observed in BL relative to CN. Comparison of  $I$ -band light curves from different explosion models could further develop this discussion.

Taken together, our results provide new observational evidence that the diversity of the  $I$ -band secondary maximum is best explained within a near- $M_{\text{Ch}}$  delayed-detonation framework, which naturally accounts for the observationally inferred anti-correlation between  $^{56}\text{Ni}$  and stable IGEs. While alternative interpretations (e.g., the sub- $M_{\text{Ch}}$  double-detonation) cannot be fully excluded, the predicted positive correlation in those models is inconsistent with our data, except possibly for the BL subclass where additional factors such as asymmetry or mixing may play a role.

#### 5.4 Diversity of the late-time $I$ -band tail slope

To further search for photometric indicators that distinguish the Branch subtypes, we examined the late-time decline in units of magnitude per day by fitting a straight line to data at  $t_{B,\text{max}} \geq 40$  days, again discarding any SNe with visibly poor fits. Figure 12 illustrates the slope distribution, where CL objects occupy a distinct locus with systematically gradual declines compared to BL, CN, or SS. This clear separation implies a practical photometric criterion; by measuring the  $I$ -band slope from just two observations beyond 40 days after B-band maximum, one can efficiently identify CL type events.

We cannot conclude exactly what causes the gradual slope seen in CL events, because  $I$ -band spectra of the SNe Ia used for the CL average light curves at  $t_{B,\text{max}} > 50\text{d}$  were unavailable for this sample. However, it is likely to be from emission features, because in this phase the ejecta has already become optically thin, allowing the contribution of emission lines to the luminosity to be dominant. In three CL SNe Ia that were not used in the average light curves, a strong emission feature at  $\sim 7,200 \text{ \AA}$  is seen and may have been present in other SNe Ia in the same subgroup (figure 13). Outside of our sample, Srivastav et al. (2017) found a similar feature in the  $+93.9 \text{ d}$  spectrum of SN 2015bp, which is a CL SN Ia with a secondary maximum, likely falling within the sample consisting the CL average light curve. Future studies could statistically confirm this unique characteristic of CL SNe Ia. Identifying this line is beyond the scope of this paper; however, it is worth noting that similar lines are seen in 1991bg-like SNe Ia (Filippenko et al. 1992; Mazzali et al. 1997). In these studies, the feature is thought to be a blend of [Fe II], [Ni II], and [Ca II] lines. Especially for calcium, the existence of the Ca II line at  $\sim 8,500 \text{ \AA}$  in the spec-

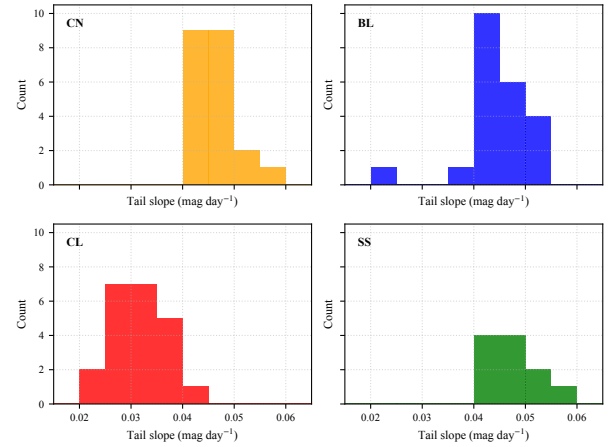


Fig. 12: Normalized histogram of the  $I$ -band tail slope measured at  $t_{B,\text{max}} \geq 40$  days, again color-coded by subclass. The CL events (red) occupy a distinct, more gradual locus compared to BL (blue), CN (orange), and SS (green). Alt text: An ensemble of four panels, corresponding to each Branch subtype. Each panel is a histogram. The x axis shows the tail slope in units of magnitude per day. The y axis shows the number of supernovae.

trum of SN 2006mr implies that the [Ca II] line is at least a portion of this feature. In the NIR, [Ni II] lines of subluminous SNe Ia have been detected as early as  $\sim 50$  days after B-band maximum (Kumar et al. 2025). If an optical counterpart of [Ni II] can be identified in the spectrum, given that the phase is well over the half-life of  $^{56}\text{Ni}$ , it would imply that stable nickel is synthesized in a majority of CL SNe Ia, favoring near- $M_{\text{Ch}}$  progenitors with a high central density, which would be consistent with our results.

## 6 Conclusion

In this study, we have constructed mean  $UBVRI$  light curve templates for each Branch spectroscopic subtype (CN, BL, CL, and SS) using a sample of 109 low-redshift SNe Ia. By fitting individual light curves with a multi-band stretch method and iteratively averaging the fitted light curves, we have investigated photometric diversity from pre-maximum epochs through the late tail.

We summarize our findings as below.

- CL SNe Ia have lower stretch values and SS SNe Ia have higher stretch values across all bands ( $\bar{s}_{B,\text{CL}} = 0.802 \pm 0.073$ ,  $\bar{s}_{B,\text{SS}} = 1.146 \pm 0.063$ ). Stretch distribution of CN and BL overlap, but CN have a larger average value than BL in  $BVRI$  bands (e.g.  $\bar{s}_{B,\text{CN}} = 1.012 \pm 0.091$ ,  $\bar{s}_{B,\text{BL}} = 0.951 \pm 0.076$ ). These stretch differences likely reflect systematic variations in the  $^{56}\text{Ni}$  mass synthesized, possibly together with changes in the ejecta mass, with CL producing less and SS producing more  $^{56}\text{Ni}$ .
- The  $I$ -band exhibits the most pronounced subtype-dependent differences. In particular, the behavior of the secondary maxima varies systematically, and the CL subgroup displays a notably slower decline in the  $I$ -band tail beyond  $+40$  days.
- The maximum of the  $B - V$  color curve coincides with the secondary maximum for all subtypes, marking the transition from photosphere-powered to line-powered luminosity as the iron recombination front recedes inward.
- Synthetic light curves demonstrate that Fe II recombination dominates the  $I$ -band secondary maximum. Combined with theoretical work, the diversity of the observed timing of the sec-

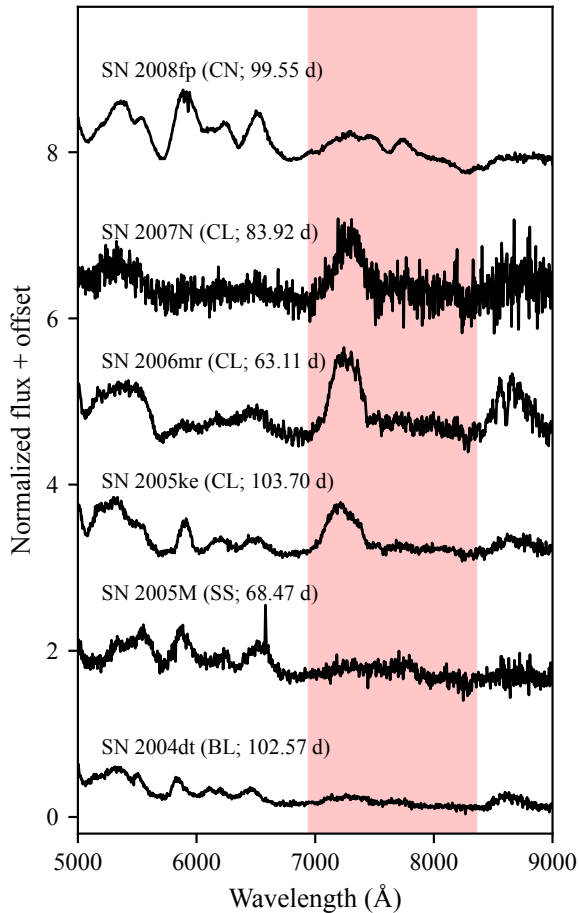


Fig. 13: Late-phase spectra of three CL objects (SN 2007N, SN 2006mr, and SN 2005ke), a CN object (SN 2008fp), a BL object (SN 2004dt), and a SS object (SN 2005M). The red region shows the wavelength range in which the transmittance of the CSP *i*-band is greater than 40% of the maximum value. Data are taken from Folatelli et al. (2013). Alt text: A graph showing six spectra. The x axis shows wavelength, and the y axis shows normalized flux with an offset for visualization.

ondary maximum is best explained by the combination of  $^{56}\text{Ni}$  mass and the amount of stable IGEs. Earlier stretch-corrected peaks in CL and BL imply larger stable-iron cores, consistent with the anti-correlation between stable IGEs and  $^{56}\text{Ni}$  expected in the near- $M_{\text{Ch}}$  delayed detonation scenario, and inconsistent with the positive correlation predicted by the sub- $M_{\text{Ch}}$  double-detonation scenario. Mixing effects may also contribute and should be tested in future work.

- The late-time *I*-band tail slope for CL SNe Ia is significantly shallower than the other subgroups. This suggests that CL SNe Ia can be distinguished from other subgroups from only two photometric observations after 40 days past *B*-band maximum. Luminosity at this phase is powered by emission lines, so a feature in the *I*-band is expected to cause this difference. However, we cannot confirm with this dataset because there was no available spectrum of a CL SN Ia that was well fit to the initial template at these epochs. Inspection of poorly fit SNe Ia (SNe Ia with only one peak in the *I*-band) showed a strong emission feature at  $\sim 7,200\text{\AA}$ , likely a blend of [Fe II], [Ni II], and [Ca II] lines. Future work may confirm if this feature is seen in other

CL events as well.

Our findings thus connect post-peak photometric behavior to explosion physics. In future work, using samples from large surveys such as the Nearby Supernova Factory (Aldering et al. 2002) and the Zwicky Transient Facility (Bellm et al. 2018; Dhawan et al. 2022; Rigault et al. 2025) could provide even more statistically robust constraints on the differences of evolution across various subclasses. In addition, extending these approaches to NIR bands and incorporating detailed modeling of mixing and electron capture effects will further disentangle the complex diversity seen in SNe Ia.

## Acknowledgments

We thank the anonymous referee for the valuable and constructive comments, which greatly helped to improve the clarity and robustness of this work. This research has made use of the CfA Supernova Archive, which is funded in part by the National Science Foundation through grant AST 0907903.

## Funding

This work was financially supported by Grants-in-Aid for Scientific Research (KAKENHI) of Japan Society for the Promotion of Science (JSPS) numbers 18H05223, 21H04491, 23H05432, 24H01810, 24K21204, and 24KK0070. This work was also supported by JSPS Bilateral Program Number JPJSBP 120227709.

## Appendix 1 Fitting results for each SN Ia

Table 5 summarizes the light curve fitting results for the SN Ia sample.

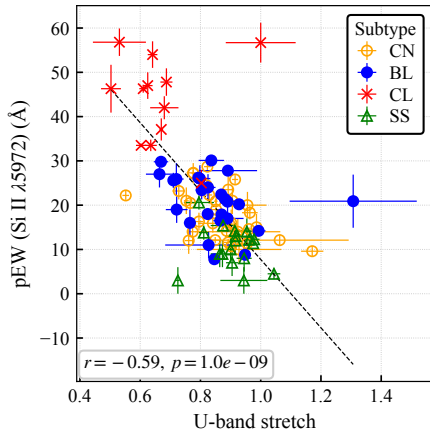
## Appendix 2 Correlation between stretch and pEW parameters

This section compiles *U*, *B*, *R*, and *I*-band plots of stretch versus the pEWs of Si II  $\lambda 5972$ ,  $\lambda 6355$ , and their ratio (figures 14–17). The *V*-band plots are presented in the main text (see subsection 4.1).

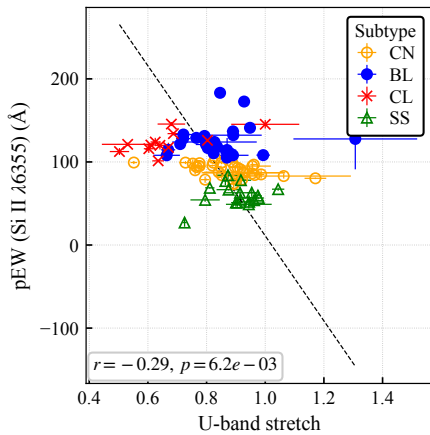
We also list the Pearson correlation coefficients ( $r$ ) for these plots, when evaluated separately for each Branch subtype and band (table 6).

## Appendix 3 Individual light curves used to construct the average templates

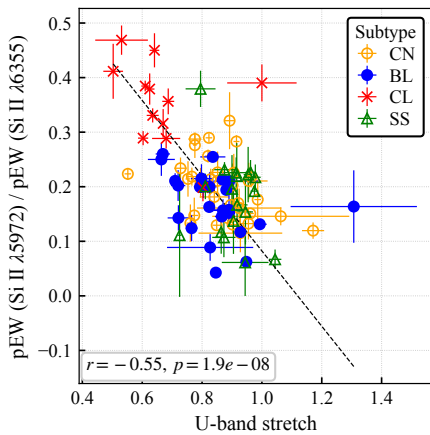
This section presents the individual *UBVRI* light curves after the first iteration (fitting to the TAK08 template) used to construct the average light curves shown in figures 5. In figure 18, all fitted light curves are overplotted in a single panel for each band and subtype.



(a) *U*-band stretch vs. pEW (Si II  $\lambda 5972$ )

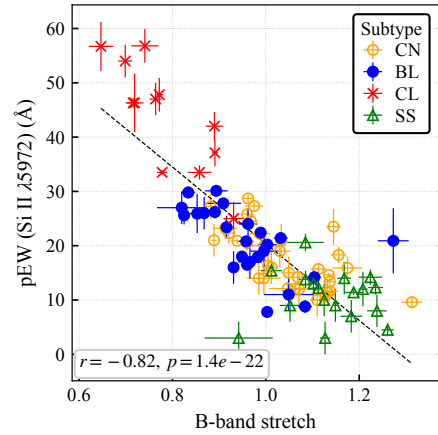


(b) *U*-band stretch vs. pEW (Si II  $\lambda 6355$ )

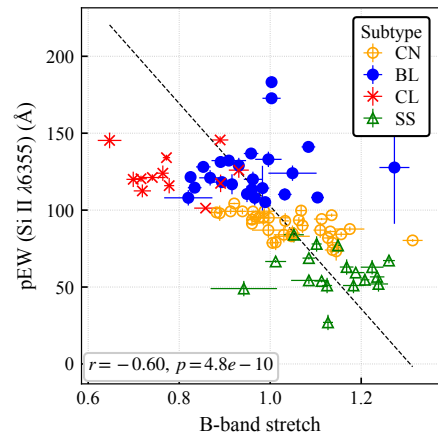


(c) *U*-band stretch vs. pEW ratio of Si II  $\lambda 5972$  and  $\lambda 6355$

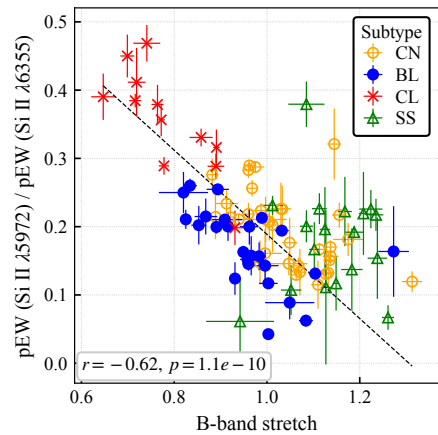
Fig. 14: Correlation between *U*-band stretch and the pEW of (a) Si II  $\lambda 5972$ , (b) Si II  $\lambda 6355$ , and (c) their ratio. The dashed line in each panel shows the best fit linear relation obtained with orthogonal distance regression. The Pearson coefficient  $r$  and  $p$ -value are also shown. Alt text: A figure consisting of three panels. All panels have *U*-band stretch as the x axis. The y axes show the pseudo-equivalent widths of the Si II line at 6355 Angstroms, the Si II line at 5972 Angstroms, and the ratio of the two lines, for each panel.



(a) *B*-band stretch vs. pEW (Si II  $\lambda 5972$ )

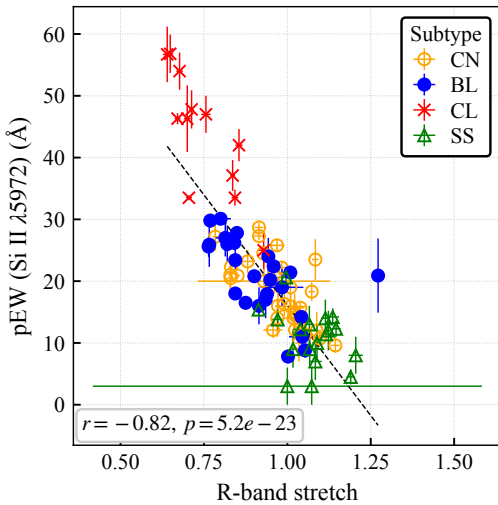


(b) *B*-band stretch vs. pEW (Si II  $\lambda 6355$ )

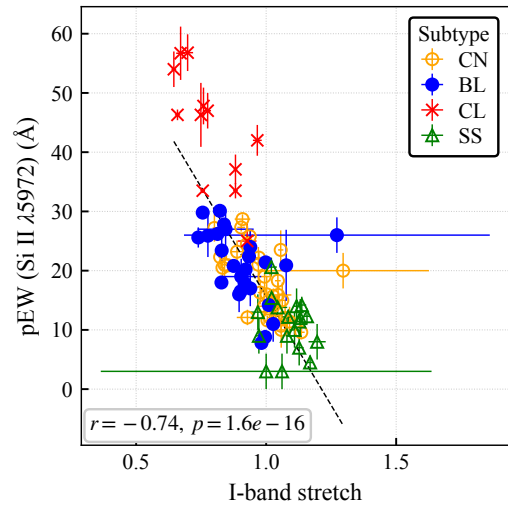


(c) *B*-band stretch vs. pEW ratio of Si II  $\lambda 5972$  and  $\lambda 6355$

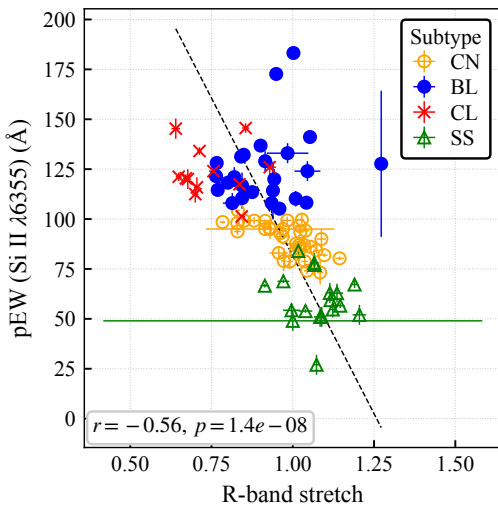
Fig. 15: The same as figure 14, but for the *B*-band. Alt text: A figure consisting of three panels. All panels have *B*-band stretch as the x axis. The y axes show the pseudo-equivalent widths of the Si II line at 6355 Angstroms, the Si II line at 5972 Angstroms, and the ratio of the two lines, for each panel.



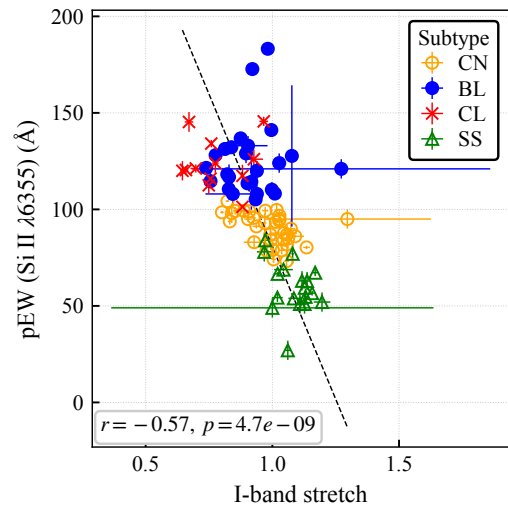
(a) *R*-band stretch vs. pEW (Si II  $\lambda$ 5972)



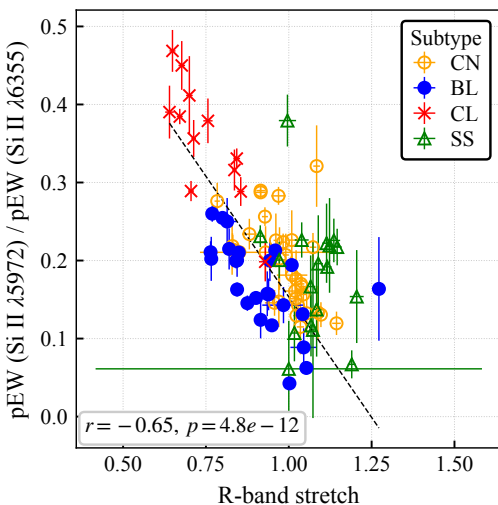
(a) *I*-band stretch vs. pEW (Si II  $\lambda$ 5972)



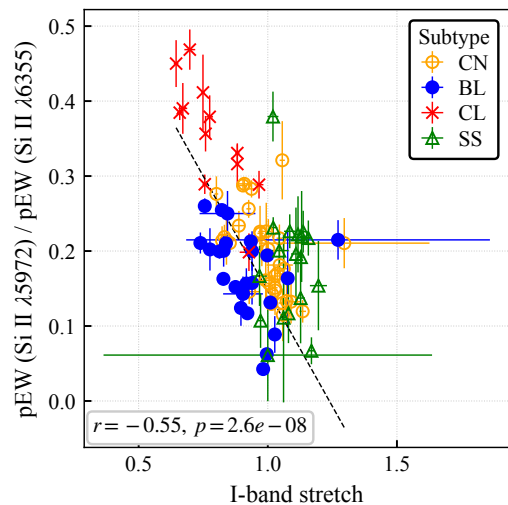
(b) *R*-band stretch vs. pEW (Si II  $\lambda$ 6355)



(b) *I*-band stretch vs. pEW (Si II  $\lambda$ 6355)



(c) *R*-band stretch vs. pEW ratio of Si II  $\lambda$ 5972 and  $\lambda$ 6355



(c) *I*-band stretch vs. pEW ratio of Si II  $\lambda$ 5972 and  $\lambda$ 6355

Fig. 16: The same as figure 14, but for the *R*-band. Alt text: A figure consisting of three panels. All panels have *R*-band stretch as the x axis. The y axes show the pseudo-equivalent widths of the Si II line at 6355 Angstroms, the Si II line at 5972 Angstroms, and the ratio of the two lines, for each panel.

Fig. 17: The same as figure 14, but for the *I*-band. Alt text: A figure consisting of three panels. All panels have *I*-band stretch as the x axis. The y axes show the pseudo-equivalent widths of the Si II line at 6355 Angstroms, the Si II line at 5972 Angstroms, and the ratio of the two lines, for each panel.

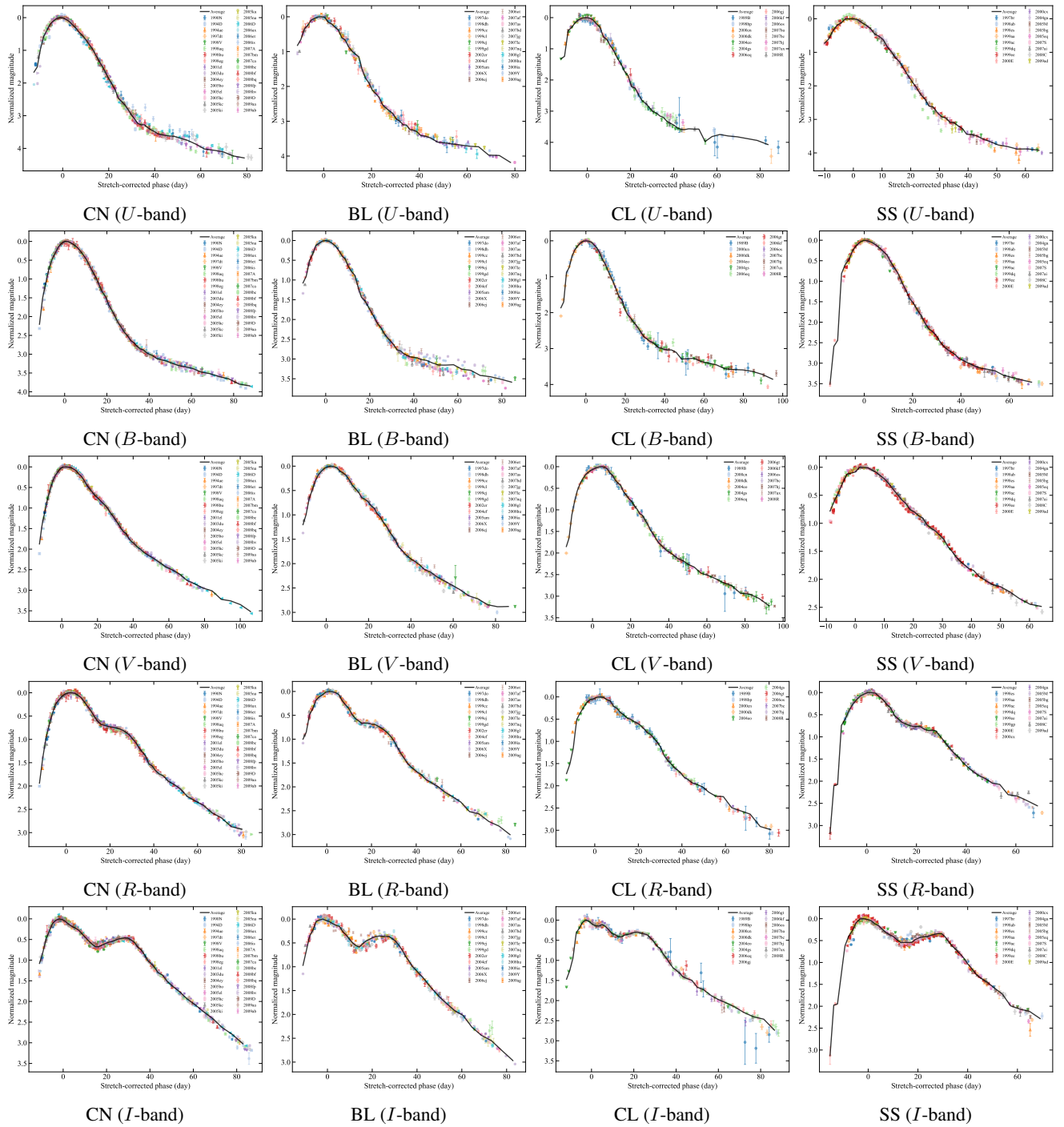


Fig. 18: Individual  $UBVRI$  light curves used to construct the averaged templates for each Branch subtype. Each panel shows all fitted light curves with the resulting averaged template overplotted (black solid line). Rows correspond to photometric bands ( $U$ ,  $B$ ,  $V$ ,  $R$ ,  $I$ ), and columns correspond to Branch subtypes (CN, BL, CL, SS). These plots illustrate the data coverage and intrinsic dispersion within each subgroup. Alt text: A 5x4 grid showing all Branch subtypes (CN, BL, CL, SS) in columns and photometric bands (U, B, V, R, I) in rows. Colored markers show the individual light curves, and solid black lines show the averaged light curves.

## References

Aldering, G., Riess, A., Antilogus, P. et al. 2002, Proc. SPIE, 4836, 61  
 Anupama, G. C., Sahu, D. K., & Jose, J. 2005, A&A, 429, 667  
 Arnett, W. D. 1982, ApJ, 253, 785  
 Bellm, E. C., Kulkarni, S. R., Graham, M. J., et al. 2018, PASP, 131, 995  
 Benetti, S., Cappellaro, E., Mazzali, P. A., et al. 2005, ApJ, 623, 1011  
 Bessell, M. S. 1990, PASP, 102, 1181

Blondin, S., Matheson, T., Kirshner, R. P., et al. 2012, AJ, 143, 5, 126  
 Blondin, S., Dessart, L., Hillier, D. J., et al. 2013, MNRAS, 429, 3, 2127  
 Blondin, S., Bravo, E., Timmes, F. X., et al. 2022, A&A, 660, A96  
 Branch, D., Dang, L. C., Hall, N., et al. 2006, PASP, 118, 560  
 Branch, D., Dang, L. C., & Baron, E. 2009, PASP, 121, 238  
 Brout, D., Scolnic, D., Popovic, B., et al. 2022, ApJ, 938, 110  
 Burgaz, U., Maeda, K., Kalomeni, B., et al. 2021, MNRAS, 502, 3, 4112  
 Burns, C. R., Stritzinger, M., Phillips, M. M., et al. 2014, ApJ, 789, 32

- Childress, Michael J., Hillier, D. John, Seitzzahl, Ivo, et al. 2019, *MNRAS*, 454, 4, 3816
- Deckers, M., Maguire, K., Shingles, L., et al. 2025, *A&A*, 694, A12
- Dhawan, S., Leibundgut, B., Spyromilio, J., et al. 2015, *MNRAS*, 448, 2, 1345
- Dhawan, S., Leibundgut, B., Spyromilio, J., et al. 2017, *A&A*, 602, A118, 7
- Dhawan, S., Goobar, A., Smith, M., et al. 2022, *MNRAS*, 510, 2, 2228
- Filippenko, A. V., Richmond, M. W., Branch, D., et al. 1992, *AJ*, 104, 4, 1543
- Folatelli, G., Morrell, N., Phillips, M. M., et al. 2013, *ApJ*, 773, 53
- Foley, R. J., Sanders, N. E., & Kirshner, R. P. 2011, *ApJ*, 742, 89
- Foreman-Mackey, D., Hogg, D. W., Dustin, L., et al. 2013, *PASP*, 125, 925, 306
- Garnavich, P. M., et al. 2004, *ApJ*, 613, 1120
- Hachinger, S., Mazzali, P. A., & Benetti, A. 2006, *MNRAS*, 370, 1, 299
- Hsiao, E., Conley, A., Howell, D. A., et al. 2007, *ApJ*, 663, 1187
- Iben, I., Jr., & Tutukov, A. V. 1984, *ApJ*, 54, 335
- Iwamoto, K., Franziska, B., Nomoto, K., et al. 1999, *ApJS*, 125, 2, 439
- Jack, D., Baron, E., & Hauschildt, P. H. 2015, *MNRAS*, 449, 4, 3581
- Jha, S., et al. 1999, *ApJS*, 125, 73
- Jha, S., Kirshner, R. P., Challis, P., et al. 2006, *AJ*, 131, 527
- Kasen, 2006, *ApJ*, 649, 939
- Kelly, P. L., Malcolm, H., Burke, D. L., et al. 2010, *AJ*, 715, 2, 743
- Kim, A., Goobar, A., & Perlmutter, S. 1996, *PASP*, 108, 190
- Krisciunas, K., et al. 2003, *AJ*, 125, 166
- Krisciunas, K., Contreras, C., Burns, C. R., et al. 2017, *AJ*, 154, 211
- Kromer, M., Sim, S. A., Fink, M., et al. 2010, *ApJ*, 719, 2, 1067
- Krueger, B. K., Jackson, A. P., Townsley, D. M. 2010, *ApJL*, 719, L5
- Kumar, S., Hsiao, E. Y., Ashall, C., et al. 2025, arXiv:2504.17134 [astro-ph.HE]
- Lach, F., Callan, F. P., Sim, S. A., et al. 2022, *A&A*, 657, A27
- Lira, P. 1995, Masters thesis, Univ. Chile
- Lira, P., et al. 1998, *AJ*, 115, 234
- Maeda, K., Benetti, S., Stritzinger, M., et al. 2010a, *Nature*, 466, 82
- Maeda, K., Taubenberger, S., Sollerman, J., et al. 2010b, *ApJ*, 708, 2, 1703
- Maeda, K., Röpke, F. K., Fink, M., et al. 2010c, *ApJ*, 712, 624
- Maeda, K., & Terada, Y. 2016, *Int. J. Mod. Phys. D*, 25, 1630024, doi:10.1142/S021827181630024X
- Magee, M. R., Sim, S. A., Kotak, R., et al. 2018, *A&A*, 614, A115
- Mazzali, P. A., Chugai, N., Turatto, M., et al. 1997, *MNRAS*, 284, 1, 151
- Mazzali, P. A., Benetti, S., Altavilla, G., et al. 2005, *ApJ*, 623, L37
- Mazzali, P. A., Röpke, Friedrich K., Benetti, Stefano, et al. 2007, *Science*, 315, 5813, 825
- Mazzali, P. A., Sullivan, A., Filippenko, A. V., et al. 2015, *MNRAS*, 450, 3, 2631
- Nomoto, K. 1982, *ApJ*, 253, 798
- Nugent, P., Phillips, M., Baron, E., et al. 1995, *ApJL*, 455, L147
- Nugent, P., Kim, A., & Perlmutter, S. 2002, *PASP*, 114, 803
- Ogawa, M., Maeda, K., & Kawabata, M. 2023, *ApJ*, 955, 49
- Pan, Y.-C., Jheng, Y.-S., Jones, D. O., et al. 2024, *MNRAS*, 532, 2, 1887
- Papadogiannakis, Seméli, Dhawan, Suhail, Morosin, Roberta, et al. 2019, *MNRAS*, 485, 2, 2343
- Perlmutter, S., Aldering, G., Goldhaber, G., et al. 1999, *ApJ*, 517, 565
- Phillips, M. M. 1993, *Astrophysical Journal Letters*, 413, L105
- Phillips, M. M., Lira, P., Suntzeff, N. B., et al. 1999, *AJ*, 118, 1766
- Pignata, G., et al. 2004, *MNRAS*, 355, 178
- Polin, A., Nugent, P., & Kasen, D. 2019, *ApJ*, 873, 84
- Richardson, D., Jenkins III, R. L., Wright, J., et al. 2014, *AJ*, 147, 118
- Richmond, M. W., et al. 1995, *AJ*, 109, 2121
- Riess, A. G., Press, W. H., & Kirshner, R. P. 1996, *ApJ*, 473, 88
- Riess, A. G., Filippenko, A. V., Challis, P., et al. 1998, *AJ*, 116, 1009
- Riess, A. G., et al. 2005, *AJ*, 627, 579
- Rigault, M., Smith, M., Goobar, A., et al. 2025, *A&A*, 694, A1
- Ruiz-Lapuente, P., Cappellaro, E., Turatto, M., et al. 1992, *ApJL*, 387, L33
- Saselli, M., Mazzali, P. A., Pian, E., et al. 2014, *MNRAS*, 445, 1, 711
- Scalzo, R. A., Parent, E., Burns, C., et al. 2019, *MNRAS*, 483, 1, 628
- Schlafly, E. F., & Finkbeiner, D. P. 2011, *AJ*, 737, 103
- Scolnic, D. M., Jones, D. O., Rest, A., et al. 2018, *ApJ*, 859, 2
- Seitzzahl, I. R., Ciaraldi-Schoolmann, F., and Röpke, F. K. 2011, *MNRAS*, 414, 3, 2709
- Seitzzahl, I. R., Ciaraldi-Schoolmann, F., Röpke, F. K., et al. 2013, *MNRAS*, 429, 2, 1156
- Shen, K. J., & Bildsten, L. 2014, *ApJ*, 785, 1, 61
- Spergel, D. N., Bean, R. Doré, O., et al. 2007, *ApJS*, 170, 377
- Srivastav, S., Anupama, G. C., Sahu, D. K., et al. 2017, *MNRAS*, 466, 2, 2436
- Stehle, M., Mazzali, P. A., Benetti, S., et al. 2005, *MNRAS*, 360, 4, 1231
- Stritzinger, M., et al. 2002, *AJ*, 124, 2100
- Stritzinger, M. D., Phillips, M. M., Boldt, L. N., et al. 2011, *AJ*, 142, 156
- Takanashi, N., Doi, M., & Yasuda, N. 2008, *MNRAS*, 389, 1577
- Taubenberger, S., Hachinger, S., Pignata, G., et al. 2008, *MNRAS*, 385, 1, 75
- Tripp, R. 1998, *A&A*, 331, 815
- Turatto, M., Benetti, S., Cappellaro, E., et al. 1996, *MNRAS*, 283, 1, 1
- Wang, X., Wang, L., Filippenko, A. V., et al. 2013, *Science*, 340, 6129, 170
- Webbink, R. F. 1984, *ApJ*, 277, 355
- Wells, L. A., et al. 1994, *AJ*, 108, 2233
- Whelan, J. & Iben, I., Jr. 1973, *ApJ*, 186, 1007
- Woosley, S. E., & Weaver, T. A. 1995, *ApJS*, 101, 181
- Woosley, S. E., & Kasen, D. 2011, *ApJ*, 734, 1, 38
- Zhao, X., Wang, X., Maeda, K., et al. 2015, *ApJS*, 220, 20
- Zhao, X., Maeda, K., Wang, X., et al. 2016, *ApJ*, 826, 211
- Zhao, X., Maeda, K., Wang, X., et al. 2021, *MNRAS*, 503, 4, 4667

Table 5: Branch subtype, data sample, heliocentric redshift, best-fit stretch values, and the reduced chi-square for each individual SN Ia. Uncertainties are given in parentheses.

SN name	Subtype	Reference	$z$	$s_U^{\text{fit}}$	$s_B^{\text{fit}}$	$s_V^{\text{fit}}$	$s_R^{\text{fit}}$	$s_I^{\text{fit}}$	$\chi_{\text{red}}^2$
SN 1989B	CL	(1)	0.002	0.803 (0.016)	0.931 (0.023)	0.929 (0.013)	0.929 (0.018)	0.927 (0.042)	0.710
SN 1990N	CN	(2)	0.003	0.761 (0.006)	1.071 (0.006)	1.049 (0.009)	1.088 (0.007)	1.073 (0.005)	2.384
SN 1991T	SS	(2)	0.006	0.725 (0.023)	1.127 (0.005)	1.067 (0.004)	1.073 (0.003)	1.061 (0.004)	3.077
SN 1994D	CN	(3)	0.002	0.753 (0.013)	0.889 (0.002)	0.797 (0.005)	0.829 (0.002)	0.840 (0.001)	1.603
SN 1994ae	CN	(4)	0.004	0.928 (0.118)	1.110 (0.010)	1.014 (0.009)	1.035 (0.006)	1.058 (0.006)	0.663
SN 1997br	SS	(5)	0.007	0.775 (0.176)	0.873 (0.275)	1.067 (0.190)	1.029 (0.133)	0.981 (0.082)	2.299
SN 1997cn	CL	(5)	0.016	1.210 (0.366)	1.184 (0.093)	0.828 (0.101)	0.673 (0.040)	0.627 (0.095)	19.246
SN 1997do	BL	(5)	0.010	0.837 (0.039)	1.011 (0.014)	1.035 (0.010)	1.059 (0.008)	1.074 (0.005)	0.781
SN 1997dt	CN	(5)	0.007	0.924 (0.045)	0.996 (0.043)	0.996 (0.045)	1.019 (0.019)	0.992 (0.041)	1.350
SN 1998V	CN	(5)	0.018	0.852 (0.015)	1.030 (0.011)	0.967 (0.006)	1.009 (0.008)	0.994 (0.009)	0.597
SN 1998ab	SS	(5)	0.027	0.762 (0.124)	0.992 (0.015)	1.046 (0.008)	1.086 (0.009)	1.055 (0.007)	2.287
SN 1998aq	CN	(4)	0.004	0.902 (0.031)	1.012 (0.005)	0.932 (0.004)	0.972 (0.005)	1.002 (0.004)	1.533
SN 1998bp	CL	(5)	0.010	0.641 (0.013)	0.699 (0.011)	0.684 (0.007)	0.677 (0.006)	0.645 (0.005)	3.359
SN 1998bu	CN	(6)	0.003	0.906 (0.007)	1.033 (0.004)	0.931 (0.003)	0.961 (0.005)	0.970 (0.004)	0.570
SN 1998dh	BL	(5)	0.009	0.825 (0.020)	0.962 (0.008)	0.926 (0.006)	0.943 (0.007)	0.939 (0.005)	0.314
SN 1998ec	BL	(5)	0.020	0.827 (0.082)	1.049 (0.069)	0.915 (0.019)	1.045 (0.026)	1.027 (0.043)	0.694
SN 1998eg	CN	(5)	0.025	0.956 (0.055)	0.997 (0.038)	0.919 (0.029)	0.930 (0.103)	1.296 (0.482)	1.163
SN 1998es	SS	(5)	0.011	0.905 (0.021)	1.183 (0.016)	1.032 (0.010)	1.084 (0.015)	1.127 (0.012)	0.598
SN 1999aa	SS	(5)	0.014	0.954 (0.007)	1.168 (0.007)	1.070 (0.006)	1.114 (0.007)	1.117 (0.006)	0.805
SN 1999ac	SS	(5)	0.009	0.873 (0.037)	1.052 (0.009)	0.982 (0.003)	1.017 (0.004)	0.972 (0.005)	1.648
SN 1999by	CL	(7)	0.002	0.682 (0.060)	0.661 (0.030)	0.646 (0.008)	0.656 (0.010)	0.605 (0.005)	12.339
SN 1999cc	BL	(5)	0.031	0.798 (0.057)	0.868 (0.016)	0.827 (0.011)	0.820 (0.010)	1.272 (0.379)	2.337
SN 1999cl	BL	(5)	0.008	0.721 (0.032)	0.996 (0.023)	0.970 (0.030)	0.984 (0.074)	0.904 (0.064)	0.691
SN 1999dq	SS	(5)	0.014	0.900 (0.007)	1.125 (0.005)	1.053 (0.005)	1.089 (0.006)	1.109 (0.009)	0.942
SN 1999ee	SS	(8)	0.011	0.864 (0.002)	1.149 (0.002)	1.052 (0.002)	1.067 (0.002)	1.080 (0.002)	0.884
SN 1999ej	BL	(5)	0.014	0.664 (0.069)	0.820 (0.038)	0.797 (0.056)	0.814 (0.419)	0.844 (0.135)	1.090
SN 1999gd	BL	(5)	0.019	0.890 (0.067)	0.966 (0.015)	0.900 (0.009)	0.935 (0.009)	0.939 (0.017)	1.474
SN 1999gh	BL	(5)	0.008	1.000 (0.181)	0.941 (0.060)	0.688 (0.057)	1.100 (0.204)	0.616 (0.855)	19.774
SN 1999gp	SS	(5)	0.027	0.945 (0.017)	1.238 (0.010)	1.146 (0.010)	1.205 (0.013)	1.196 (0.018)	1.414
SN 2000B	BL	(5)	0.020	1.477 (0.222)	1.157 (0.153)	0.876 (0.062)	0.872 (0.089)	1.085 (0.150)	40.265
SN 2000E	SS	(5)	0.005	0.917 (0.006)	1.102 (0.003)	1.002 (0.003)	1.066 (0.006)	0.968 (0.012)	1.866
SN 2000cn	CL	(5)	0.023	0.743 (0.011)	0.773 (0.194)	0.756 (0.011)	0.771 (0.015)	0.844 (0.449)	1.132
SN 2000cx	SS	(5)	0.008	0.944 (0.041)	0.942 (0.023)	1.000 (0.000)	1.000 (0.000)	1.000 (0.000)	0.155
SN 2000dk	CL	(5)	0.017	0.625 (0.010)	0.764 (0.005)	0.765 (0.007)	0.756 (0.008)	0.775 (0.018)	1.538
SN 2001el	CN	(9)	0.004	0.774 (0.024)	0.985 (0.004)	1.016 (0.002)	0.970 (0.005)	1.028 (0.003)	0.725
SN 2002er	BL	(10)	0.009	0.765 (0.014)	0.931 (0.008)	0.918 (0.009)	0.915 (0.007)	0.896 (0.005)	0.569
SN 2003du	CN	(11)	0.006	0.986 (0.010)	1.049 (0.008)	0.987 (0.007)	1.022 (0.005)	1.062 (0.021)	1.154
SN 2004dt	BL	(12)	0.020	0.928 (0.219)	1.003 (0.086)	0.815 (0.024)	0.949 (0.018)	0.921 (0.014)	2.722
SN 2004ef	BL	(12)	0.031	0.793 (0.006)	0.891 (0.002)	0.833 (0.002)	0.841 (0.001)	0.813 (0.001)	0.900
SN 2004eo	CL	(12)	0.016	0.670 (0.035)	0.891 (0.005)	0.847 (0.005)	0.836 (0.005)	0.882 (0.003)	2.717
SN 2004ey	CN	(12)	0.016	0.887 (0.003)	1.068 (0.003)	0.986 (0.002)	1.028 (0.002)	1.017 (0.001)	0.541
SN 2004gs	CL	(12)	0.027	0.687 (0.024)	0.772 (0.005)	0.689 (0.006)	0.713 (0.003)	0.759 (0.004)	2.851
SN 2004gu	SS	(12)	0.046	1.044 (0.016)	1.261 (0.007)	1.163 (0.006)	1.190 (0.005)	1.169 (0.005)	1.423
SN 2005M	SS	(12)	0.025	0.916 (0.007)	1.208 (0.005)	1.107 (0.004)	1.123 (0.003)	1.131 (0.002)	0.829
SN 2005am	BL	(12)	0.008	0.710 (0.005)	0.825 (0.003)	0.754 (0.003)	0.764 (0.003)	0.739 (0.002)	0.915
SN 2005bg	SS	(12)	0.023	0.962 (0.009)	1.113 (0.005)	1.002 (0.009)	1.039 (0.007)	1.085 (0.007)	1.133
SN 2005bl	CL	(12)	0.024	0.975 (0.085)	0.976 (0.084)	0.651 (0.008)	0.636 (0.011)	1.277 (0.118)	35.609
SN 2005bo	CN	(12)	0.014	0.728 (0.009)	0.913 (0.011)	0.867 (0.017)	0.881 (0.012)	0.888 (0.008)	0.239
SN 2005el	CN	(12)	0.015	0.766 (0.008)	0.960 (0.003)	0.790 (0.004)	0.830 (0.003)	0.832 (0.001)	0.711
SN 2005eq	SS	(12)	0.029	0.978 (0.006)	1.235 (0.006)	1.123 (0.006)	1.146 (0.007)	1.157 (0.004)	0.894
SN 2005hc	CN	(12)	0.046	0.964 (0.014)	1.156 (0.007)	1.025 (0.004)	1.073 (0.004)	1.045 (0.005)	0.677
SN 2005kc	CN	(12)	0.015	0.915 (0.005)	0.960 (0.005)	0.930 (0.004)	0.969 (0.005)	0.937 (0.004)	1.425
SN 2005ke	CL	(12)	0.005	0.799 (0.047)	0.920 (0.025)	0.670 (0.004)	1.116 (0.020)	0.599 (0.018)	22.223
SN 2005ki	CN	(12)	0.019	0.829 (0.045)	0.921 (0.007)	0.805 (0.005)	0.831 (0.003)	0.823 (0.002)	0.814
SN 2005ku	CN	(12)	0.045	1.063 (0.161)	1.047 (0.022)	1.016 (0.023)	0.957 (0.025)	0.928 (0.036)	0.959
SN 2005na	CN	(12)	0.026	0.795 (0.009)	1.005 (0.005)	0.872 (0.017)	0.991 (0.003)	0.977 (0.003)	0.661
SN 2006D	CN	(12)	0.009	0.776 (0.445)	0.882 (0.046)	0.894 (0.502)	0.784 (0.026)	0.801 (0.094)	2.858
SN 2006X	BL	(12)	0.005	0.846 (0.005)	1.003 (0.011)	0.990 (0.004)	1.002 (0.002)	0.982 (0.001)	3.758

Table 5: (Continued)

SN name	Subtype	Reference	$z$	$s_U^{\text{fit}}$	$s_B^{\text{fit}}$	$s_V^{\text{fit}}$	$s_R^{\text{fit}}$	$s_I^{\text{fit}}$	$\chi_{\text{red}}^2$
SN 2006ax	CN	(12)	0.017	0.849 (0.004)	1.063 (0.002)	0.993 (0.003)	1.023 (0.002)	1.014 (0.002)	0.873
SN 2006ef	BL	(12)	0.018	0.891 (0.106)	0.909 (0.027)	0.746 (0.014)	0.849 (0.036)	0.838 (0.013)	0.710
SN 2006ej	BL	(12)	0.020	0.836 (0.047)	0.894 (0.030)	0.803 (0.054)	0.800 (0.071)	0.822 (0.017)	0.434
SN 2006eq	CL	(12)	0.050	1.000 (0.104)	0.647 (0.023)	0.644 (0.021)	0.640 (0.010)	0.671 (0.016)	3.906
SN 2006et	CN	(12)	0.022	0.892 (0.011)	1.145 (0.005)	1.031 (0.005)	1.084 (0.002)	1.056 (0.005)	0.645
SN 2006fw	CN	(12)	0.083	1.225 (0.410)	1.000 (0.042)	0.939 (0.052)	0.940 (0.026)	0.989 (0.041)	8.585
SN 2006gj	CL	(12)	0.028	0.503 (0.065)	0.719 (0.016)	0.685 (0.015)	0.700 (1.419)	0.749 (0.985)	2.305
SN 2006gt	CL	(12)	0.045	0.531 (0.108)	0.741 (0.037)	0.618 (0.009)	0.649 (0.004)	0.698 (0.018)	3.903
SN 2006hx	SS	(12)	0.045	0.795 (0.214)	1.085 (0.036)	0.995 (0.011)	0.996 (0.027)	1.020 (0.169)	2.937
SN 2006is	CN	(12)	0.031	1.171 (0.032)	1.313 (0.010)	1.069 (0.003)	1.144 (0.007)	1.135 (0.005)	2.330
SN 2006kf	CL	(12)	0.021	0.603 (0.030)	0.778 (0.018)	0.708 (0.015)	0.705 (1.061)	0.756 (0.008)	1.789
SN 2006mr	CL	(12)	0.006	0.686 (0.082)	0.870 (0.015)	0.617 (0.333)	1.632 (0.175)	0.525 (0.101)	35.597
SN 2006os	CL	(12)	0.033	0.680 (0.035)	0.890 (0.009)	0.882 (0.009)	0.855 (0.005)	0.966 (0.015)	1.820
SN 2006ot	BL	(12)	0.053	1.307 (0.166)	1.273 (0.044)	1.139 (0.022)	1.272 (0.036)	1.077 (0.017)	3.908
SN 2007A	CN	(12)	0.018	0.841 (0.021)	1.175 (0.017)	0.995 (0.017)	1.010 (0.012)	1.046 (0.009)	0.849
SN 2007N	CL	(12)	0.013	0.848 (0.255)	1.015 (0.027)	0.630 (0.006)	0.563 (0.037)	1.430 (0.151)	15.897
SN 2007S	SS	(12)	0.014	0.975 (0.005)	1.188 (0.011)	1.110 (0.008)	1.116 (0.004)	1.128 (0.003)	1.639
SN 2007af	BL	(12)	0.005	0.869 (0.006)	0.989 (0.005)	0.920 (0.003)	0.959 (0.002)	0.934 (0.002)	0.768
SN 2007ai	SS	(12)	0.032	0.914 (0.060)	1.224 (0.017)	1.114 (0.015)	1.136 (0.016)	1.137 (0.012)	0.852
SN 2007al	CL	(12)	0.012	0.512 (0.021)	0.806 (0.052)	0.622 (0.011)	0.552 (0.005)	0.502 (0.475)	18.490
SN 2007as	BL	(12)	0.018	0.890 (0.013)	0.958 (0.007)	0.876 (0.003)	0.901 (0.003)	0.875 (0.002)	0.543
SN 2007ax	CL	(12)	0.007	0.914 (0.073)	1.001 (0.089)	0.593 (0.024)	0.984 (1.338)	0.492 (0.814)	71.515
SN 2007ba	CL	(12)	0.039	0.707 (0.016)	0.659 (0.007)	0.607 (0.008)	0.691 (0.009)	0.668 (0.011)	6.602
SN 2007bc	CL	(12)	0.021	0.635 (0.007)	0.858 (0.012)	0.815 (0.003)	0.843 (0.003)	0.882 (0.002)	1.314
SN 2007bd	BL	(12)	0.031	0.866 (0.013)	0.960 (0.006)	0.841 (0.007)	0.875 (0.004)	0.902 (0.007)	2.118
SN 2007bm	CN	(12)	0.006	0.776 (0.007)	0.975 (0.003)	0.911 (0.003)	0.915 (0.003)	0.904 (0.002)	0.684
SN 2007ca	CN	(12)	0.014	0.955 (0.014)	1.132 (0.004)	1.010 (0.004)	1.054 (0.003)	1.090 (0.005)	1.419
SN 2007hj	CL	(12)	0.014	0.612 (0.007)	0.757 (0.008)	0.679 (0.007)	0.686 (0.006)	0.704 (0.016)	5.533
SN 2007jg	BL	(12)	0.037	0.870 (0.025)	0.983 (0.009)	0.880 (0.011)	0.939 (0.009)	0.917 (0.006)	0.974
SN 2007le	BL	(12)	0.007	0.993 (0.016)	1.104 (0.004)	1.010 (0.003)	1.042 (0.002)	1.010 (0.001)	0.678
SN 2007nq	BL	(12)	0.045	0.669 (0.015)	0.834 (0.009)	0.740 (0.007)	0.769 (0.005)	0.756 (0.006)	1.069
SN 2007on	CL	(12)	0.006	0.760 (0.133)	0.895 (0.134)	0.809 (0.094)	0.597 (0.534)	0.668 (0.489)	10.111
SN 2007ux	CL	(12)	0.031	0.572 (0.012)	0.712 (0.006)	0.681 (0.006)	0.667 (0.004)	0.694 (0.005)	4.345
SN 2008C	SS	(12)	0.017	0.875 (0.026)	1.012 (0.014)	1.000 (0.010)	0.914 (0.009)	1.021 (0.010)	2.874
SN 2008R	CL	(12)	0.013	0.610 (0.009)	0.716 (0.004)	0.650 (0.003)	0.671 (0.125)	0.659 (0.006)	2.648
SN 2008ar	CN	(12)	0.026	0.552 (0.162)	0.987 (0.023)	0.964 (0.005)	0.983 (0.007)	0.972 (0.007)	3.830
SN 2008bc	CN	(12)	0.015	0.961 (0.004)	1.135 (0.002)	0.994 (0.003)	1.021 (0.003)	1.028 (0.002)	0.797
SN 2008bf	CN	(12)	0.024	0.921 (0.008)	1.137 (0.003)	0.987 (0.002)	1.037 (0.003)	1.037 (0.004)	0.830
SN 2008bq	CN	(12)	0.034	0.896 (0.013)	1.113 (0.007)	1.037 (0.006)	1.039 (0.004)	1.027 (0.006)	0.396
SN 2008fp	CN	(12)	0.006	0.892 (0.008)	1.137 (0.008)	1.008 (0.004)	1.044 (0.002)	1.005 (0.002)	0.728
SN 2008gl	BL	(12)	0.034	0.804 (0.012)	0.916 (0.004)	0.824 (0.005)	0.844 (0.004)	0.829 (0.004)	0.724
SN 2008hu	BL	(12)	0.050	0.720 (0.016)	0.853 (0.010)	0.758 (0.006)	0.766 (0.005)	0.776 (0.005)	1.836
SN 2008hv	CN	(12)	0.013	0.851 (0.012)	0.939 (0.003)	0.838 (0.003)	0.851 (0.002)	0.853 (0.002)	1.111
SN 2008ia	BL	(12)	0.022	0.824 (0.009)	0.949 (0.004)	0.830 (0.004)	0.844 (0.003)	0.828 (0.004)	0.633
SN 2009D	CN	(12)	0.025	0.902 (0.004)	1.127 (0.004)	1.039 (0.003)	1.097 (0.003)	1.057 (0.004)	0.487
SN 2009F	CL	(12)	0.013	0.576 (0.020)	0.634 (0.014)	0.576 (0.011)	0.589 (0.128)	0.545 (0.027)	14.607
SN 2009Y	BL	(12)	0.009	0.948 (0.017)	1.084 (0.010)	1.015 (0.003)	1.053 (0.002)	0.996 (0.002)	2.066
SN 2009aa	CN	(12)	0.027	0.820 (0.005)	0.968 (0.005)	0.896 (0.004)	0.928 (0.003)	0.926 (0.003)	1.138
SN 2009ab	CN	(12)	0.011	0.823 (0.096)	0.962 (0.013)	0.889 (0.009)	0.915 (0.009)	0.909 (0.080)	1.439
SN 2009ad	SS	(12)	0.028	0.811 (0.010)	1.085 (0.005)	0.970 (0.004)	0.971 (0.005)	1.044 (0.004)	1.151
SN 2009ag	BL	(12)	0.009	0.881 (0.005)	1.032 (0.003)	0.981 (0.003)	1.009 (0.002)	0.998 (0.002)	1.355

**Notes.**— References are as follows: (1) Wells (1994), (2) Lira (1998), (3) Richmond et al. (1995), (4) Riess et al. (2005), (5) Jha et al. (2006), (6) Jha et al. (1999), (7) Garnavich et al. (2004), (8) Stritzinger et al. (2002), (9) Krisciunas et al. (2003), (10) Pignata et al. (2004), (11) Anupama et al. (2005), and (12) Krisciunas et al. (2017). SNe Ia from references (1)–(11) are treated as the TAK08 sample, and those from reference (12) are treated as the CSP sample in this study.

Table 6: Pearson  $r$  and correlation significance based on  $p$ -values for stretch vs. three different pEW-related values by Branch subtype.

Band	CN	BL	CL	SS
<b>(1) pEW (Si II <math>\lambda</math>5972)</b>				
<i>U</i>	-0.49*	-0.26 <sup>‡</sup>	-0.13 <sup>§</sup>	+0.22 <sup>§</sup>
<i>B</i>	-0.68*	-0.55*	-0.48*	+0.35 <sup>§</sup>
<i>V</i>	-0.66*	-0.67*	-0.52*	-0.21 <sup>§</sup>
<i>R</i>	-0.68*	-0.63*	-0.56*	-0.20 <sup>§</sup>
<i>I</i>	-0.56*	-0.47*	-0.58*	+0.07 <sup>§</sup>
<b>(2) pEW (Si II <math>\lambda</math>6355)</b>				
<i>U</i>	-0.49 <sup>†</sup>	+0.02 <sup>§</sup>	-0.003 <sup>§</sup>	+0.47*
<i>B</i>	-0.63*	-0.40*	-0.03 <sup>§</sup>	+0.47*
<i>V</i>	-0.54*	-0.53*	-0.03 <sup>§</sup>	-0.13 <sup>§</sup>
<i>R</i>	-0.66*	-0.47*	-0.09 <sup>§</sup>	-0.03 <sup>§</sup>
<i>I</i>	-0.45*	-0.16 <sup>§</sup>	-0.14 <sup>§</sup>	+0.08 <sup>§</sup>
<b>(3) pEW (Si II <math>\lambda</math>5972) / pEW (Si II <math>\lambda</math>6355)</b>				
<i>U</i>	-0.45*	-0.35 <sup>†</sup>	-0.33 <sup>†</sup>	-0.22 <sup>‡</sup>
<i>B</i>	-0.53*	-0.59*	-0.80*	+0.04 <sup>§</sup>
<i>V</i>	-0.52*	-0.58*	-0.83*	-0.16 <sup>§</sup>
<i>R</i>	-0.52*	-0.60*	-0.82*	-0.22 <sup>§</sup>
<i>I</i>	-0.46*	-0.37*	-0.79*	-0.003 <sup>§</sup>

\*  $p < 10^{-3}$ .

†  $10^{-3} \leq p < 10^{-2}$ .

‡  $10^{-2} \leq p < 0.05$ .

§  $0.05 \leq p$ .